Nordisk kernesikkerhedsforskning
Norrænar kjarnöryggisrannsóknir
Pohjoismainen ydinturvallisuustutkimus
Nordisk kjernesikkerhetsforskning
Nordisk kärnsäkerhetsforskning
Nordic nuclear safety research

NKS-104
ISBN 87-7893-163-0

Fluid-Structure Interaction Analysis of a Water Pool under Loading Caused by a Condensation-Induced Water Hammer

Timo Pättikangas, Antti Timperi, Jarto Niemo & Timo Narumo

VTT Industrial Systems, Finland

April 2005

Abstract

A coupled fluid-structure interaction calculation was performed with Star-CD and ABAQUS, which were coupled with the ES-FSI code. The motion of the wall of a test pool during a rapid bubble collapse was solved and taken into account during the CFD calculation. A fluid-structure interaction analysis was also conducted, in which the stationary state of the pool due to a gravity load was calculated. In addition, methods for estimating pressure loads in a water pool during steam injection were investigated. The Method of Images (MOI) for calculating the pressure loads during a steam bubble collapse was implemented and tested for the POOLEX experiment. The first version of the homogeneous two-phase model was implemented for the Star-CD CFD code and tested in the quasi-stationary situation, where the steam that was blown down into a water pool was condensing inside the vertical blowdown pipe.

Key words

CFD, FE, FSI, condensation water hammer, pressure load

NKS-104
ISBN 87-7893-163-0

Electronic report, April 2005

The report can be obtained from
NKS Secretariat
NKS-775
P.O. Box 49
DK - 4000 Roskilde, Denmark

Phone +45 4677 4045
Fax +45 4677 4046
www.nks.org
e-mail nks@nks.org

RESEARCH REPORT | NO BTUO72-051332 | 4.2.2005

Fluid-Structure Interaction Analysis of a Water Pool under Loading Caused by a Condensation Induced Water Hammer

Customer: VYR, NKS

VTT TECHNICAL RESEARCH CENTRE OF FINLAND

VTT INDUSTRIAL SYSTEMS

Public	X	Registered in VTT publications register JURE	X
Confidential until / permanently			
Internal use only			

Title	
Fluid-Structure Interaction Analysis of a Water Pool under Loading Caused by a Condensation Induced Water Hammer	
Customer or financing body and order date/No. VYR, NKS	Research report No. BTUO72-051332
Project SAFIR / INTELI / INPUT	Project No. G4SU00055
Author(s) Timo Pättikangas, Antti Timperi, Jarto Niemi and Timo Narumo	No. of pages/appendices 56
Keywords CFD, FE, FSI, condensation water hammer, pressure load	

Summary

A coupled fluid-structure interaction calculation was performed with Star-CD and ABAQUS, which were coupled with the ES-FSI code. The motion of the wall of a test pool during a rapid bubble collapse was solved and taken into account during the CFD calculation. A fluid-structure interaction analysis was also conducted, in which the stationary state of the pool due to a gravity load was calculated. In addition, methods for estimating pressure loads in a water pool during steam injection were investigated. The Method Of Images (MOI) for calculating the pressure loads during a steam bubble collapse was implemented and tested for the POOLEX experiment. First version of homogeneous two-phase model was implemented for Star-CD CFD code and tested in the quasi-stationary situation, where the steam that was blown down into a water pool was condensing inside the vertical blowdown pipe.

Analysis with ES-FSI includes substructure analysis, which were examined in detail. Substructure analyses of the pool showed that computer memory requirement would be excessive, if a large substructure of the pool were used. Using a substructure with a small number of retained degrees of freedom had a deteriorative effect on the accuracy of the FSI analyses. ES-FSI was found generally more suitable for cases, in which the structural model is relatively small. Analyses with ES-FSI are limited to linear structural problems. In the FSI analyses of the pool, a too small selection of retained degrees of freedom was used. Comparison of the dynamic analysis to an earlier uncoupled case was not possible due to different initial conditions in the analyses. It was concluded that accurate FSI analysis of the pool, or similar case, can be carried out with ES-FSI. However for FSI analyses including a larger structural model, another coupling method may have to be used.

VTT TECHNICAL RESEARCH CENTRE OF FINLAND
VTT INDUSTRIAL SYSTEMS
Kemistintie 3, Espoo
P.O. Box 1704, FIN-02044 VTT
FINLAND
Tel. +358 9 4561
Fax +358 9 456 7002,
+358 9 456 5875
name.surname@vtt.fi
www.vtt.fi/tuo
Business ID 0244679-4

Date 2 February, 2005		
Rauno Rintamaa Research Manager	Antti Timperi Research Scientist	Heli Talja Checked
Distribution (customers and VTT): STUK (6), Heikki Sjövall (TVO), Arja Saarenheimo (VTT Industrial Systems), Kim Calonius (VTT Industrial Systems), Antti Timperi (VTT Industrial Systems), Timo Narumo (VTT Processes), Jarto Niemi (VTT Processes), Timo Pättikangas (VTT Processes), Heikki Pokela (VTT Processes), Markku Puustinen (LUT), Jani Laine (LUT), Pentti Varpasuo (Fortum Nuclear Services), Ville Lestinen (Fortum Nuclear Services), Petra Lundström (Fortum Nuclear Services)		
The use of the name of VTT in advertising, or publication of this report in part is allowed only by written permission from VTT.		

VTT TECHNICAL RESEARCH CENTRE OF FINLAND
VTT INDUSTRIAL SYSTEMS
Kemistintie 3, Espoo
P.O. Box 1704, FIN-02044 VTT
FINLAND
Tel. +358 9 4561
Fax +358 9 456 7002,
+358 9 456 5875
name.surname@vtt.fi
www.vtt.fi/tuo
Business ID 0244679-4

Foreword

This study is part of the INTELI (Integrity and Life Time of Reactor Circuits) project carried out in the SAFIR Programme, the Finnish Research Programme on Nuclear Power Plant Safety. This study is funded by the State Nuclear Waste Management Fund (VYR) and by the Nordic Nuclear Safety Research (NKS). The contact person in STUK is Dr. Martti Vilpas.

Interest and contribution of CD adapco Group to the project is greatly acknowledged. The authors thank Dr. David Eby for valuable discussions and for instructions and assistance in the use of ES-FSI code.

Espoo

Authors

Table of Contents

Nomenclature

c_p	specific heat capacity, J/kgK
D_e	characteristic length, m
E	Young's modulus, N/m^2
h	specific enthalpy , J/kg
h	wall heat transfer coefficient, W/m^{2}K
h_{fg}	latent heat of vaporization, J/kg
g	gravitation acceleration, m/s^2
$[K]$	tangent stiffness matrix
$[\overline{K}]$	reduced tangent stiffness matrix
k	thermal conductivity, W/mK
$\{\Delta P\}$	nodal force vector
p	pressure, Pa
Pr	Prandtl number
q	heat flux. W/m^2
Re	Reynolds number
T	temperature, K
t	time, s
$\{\Delta u\}$	displacement vector
$\{\delta u\}$	virtual displacement vector
X	mass fraction
u	velocity, m/s
δW	virtual work, J
μ	dynamic viscosity, kg/ms
μ_t	turbulent viscosity, kg/ms
α	mass proportional damping, 1/s
β	stiffness proportional damping, s
ν	Poisson's ratio
ρ	density, kg/m^3
σ	surface tension, N/m; stress, N/m^2

Superscripts

M	master degrees of freedom
S	slave degrees of freedom

Subscripts

f	saturated liquid condition
g	saturated vapor condition

Abbreviations

CFD	computational fluid dynamics
DOF	degrees of freedom
FSI	fluid-structure interaction
FE	finite element
LOCA	loss-of-coolant accident
MDOF	master degrees of freedom
MOI	method of images
SDOF	slave degrees of freedom

1 Introduction

In the POOLEX project of the Finnish Research Programme on Nuclear Power Plant Safety (SAFIR), injection of air and steam into a water pool is investigated experimentally at Lappeenranta University of Technology. In the first experimental series, air was injected into the pool through a vertical pipe submerged in water (Laine, 2002). In the second series, preliminary experiments with steam have been conducted (Laine and Puustinen, 2003; Laine and Puustinen, 2004).

Previously, one-directional FSI analyses of the pool have been performed, where the pool wall has been rigid during the computational fluid dynamics (CFD) analysis. Numerical simulations of the tests with air are presented by Calonius et al. (2003) and Pättikangas and Pokela (2003). The injection of steam was considered in Timperi et al. (2004), where a large rapidly condensing steam bubble was modelled with a single-phase CFD calculation. Different solutions for fully coupled FSI analysis were also discussed. Also in the MULTIPHYSICS project of the SAFIR programme, a large-break loss-of-coolant accident (LOCA) was analysed in a pressurised-water reactor with a one-directional FSI calculation (Pättikangas and Timperi, 2004).

The requirements for software and computer resources in FSI analyses are quite large, but software for the analyses, along with computing power, is developing rapidly. Several commercial FSI solutions, using different methods, have appeared recently. The main vendors of the commercial CFD and structural analysis codes are developing methods for performing fully coupled fluid-structure interaction calculations. Certain smaller vendors are also developing software, e.g. MpCCI and Smart Coupling, for coupling commonly used analysis codes. Star-CD has three solutions for coupling the CFD analysis with different finite element (FE) codes. The CFX-5 code can be coupled with Ansys and LS-Dyna is also available for FSI analyses. It is of importance to find methods suitable for the FSI problems found in the nuclear industry. In addition to the nuclear industry, FSI calculations are widely needed in many other industrial applications.

In the first part of the present work, three different methods for estimating the pressure loads in a water pool during steam condensation are investigated. The loads caused by a rapid condensation of a steam bubble are calculated with the method of images which consists of solving the Poisson equation with a pre-determined pressure source. A homogeneous two-phase model is implemented and tested for CFD calculations of condensation of steam in a water pool. In addition, a single-phase model previously used for collapse of a steam bubble is briefly reviewed. In this model, the rapid collapse of a steam bubble is modelled with a mass sink.

In the second part of the present work, three-dimensional FSI analysis of the water pool is carried out by using the ES-FSI code developed by CD adapco Group. The flow analysis is conducted with the Star-CD code (Anon., 2001). ABAQUS FE code (ABAQUS, 2003a) is used for solving the structural behaviour. First, fluid-structure interaction analysis of the stationary state of the pool under hydrostatic load is performed and compared to a conventional solution. Second, fluid-structure interaction analysis of a rapid collapse of a steam bubble is performed and compared to a previous analysis, where rigid pool wall was assumed. Substructure analysis is discussed in detail, since analysis with ES-FSI includes substructuring of the FE model. The main aim of the present FSI analysis is to test the applicability of the ES-FSI code to the calculation of rapid pressure transients. Another goal is to study the behaviour of the water pool with FSI calculation.

This report is organised in the following way. Section 2 contains discussion on alternative ways to calculate loads in a water pool during the injection of steam. The FSI analysis of the pool with ES-FSI is presented in Section 3. Finally, Section 4 contains a summary and conclusions on the results.

2 Alternatives for Analysing Loads in a Water Pool

In the following, three different methods for estimating the pressure loads in a water pool during a steam bubble collapse are discussed. First, the method of images is implemented in order to obtain an alternative method to CFD for estimating the loads during bubble collapse. Second, first version of homogeneous two-phase model for condensation of steam is described and implemented. Third, a simple analytical model for the bubble collapse is reviewed.

2.1 Analysis of Wall Loading with Method Of Images (MOI)

It is of interest to find analytical or numerical methods easier than direct 3D fluid flow calculation, to estimate pressure loads onto a BWR suppression pool during discharge of steam or air or during chugging phenomenon.

The potential theory offers a solid starting-point for the problem area, if the assumptions of the flow being time-independent, incompressible and free of vortices, can be justified. Those assumptions would be somewhat questionable if we were interested in detailed flow behaviour in different dynamic situations but, in this study, we only wanted to estimate the roughly the magnitude of the pressure loads onto the suppression pool walls. The potential theory will serve well for the purpose and for the accuracy level sought.

In the following, applying the Method Of Images (MOI) (Wood et al., 1980; Li and Uren, 1997; Anderson, 2000) for the problem field was studied. The method was chosen here because of its relative simplicity and robustness. Other possible methods would have been to try to solve the underlying model analytically as expansion of Green's functions eigenvalue problem or numerically by applying a suitable finite-difference scheme. However, the last alternative would have resembled the method of formulating the problem as a case of 3D fluid flow and solve it numerically by a (commercial) CFD package. This would have been in slight contradiction with the goal which was to find an *independent* estimate compared with CFD calculation, yet preferably simpler to achieve, for the pool wall loads during the LOCA event or other gas discharge of similar nature. The analytic solution based on Green's functions was postponed at this stage because of high complexity of the method. Still, it may be considered a method worth studying in the future.

In order to couple the calculated results to concrete measurement data even coarsely, the MOI is applied to the modified geometry of POOLEX test rig for which there exists measured results for air and steam discharges (Laine and Puustinen, 2003). However, the test facility is of cylindrical shape and the MOI cannot be applied exactly to such geometry. Therefore, two rectangular shaped geometries, representing equal volume and conservative volume analogies, have been chosen to be fed to the MOI. This rather radical transformation from cylindrical experimental set-up geometry can be justified by remembering that the primary aim is to estimate the *maximum* pressure load onto the pool walls. Thus, rectangular-shaped pool serves well for the purpose when the dimensions of the pool have been chosen suitably such that the distances to different directions from the steam source to the pool walls are of the same magnitude as within the experimental set-up.

2.1.1 Method Of Images

The MOI is a widely known classical hydrodynamic technique. Its idea is in expanding the real geometry to near infinity, or in practise some several ten times to each direction, by removing the walls and mirroring the geometry to form a 'tunnel' of mirrored images. When applied to 3D, the result geometry for the method is a diamond-shaped structure of imaginary pools, only the middle one being the real volume of whose properties we are interested in. This manoeuvre makes the solution to fluid flow problem to satisfy boundary conditions asymptotically when the number of mirrored pools is increased. The following assumptions have to be made to justify the use of the MOI:

- incompressible potential flow with bubble(s) represented by a point source,
- pool geometry has to be approximated by a 3D rectangular pool,
- free surface is stationary and at constant pressure and is represented by a point sink above the point source, symmetrically about the water surface,
- structures below water surface will not affect the flow field,
- the strength of point source(s), or bubble pressure and radius, have to be obtained from an independent model,
- the effect of hydrostatic head and normal air pressure is neglected, but they can be added to the result afterwards.

With these assumptions, the flow field can be described by the Poisson equation with point source S at (x', y', z'):

$$\nabla^2 p(x,y,z) = -\frac{4\pi S(x,y,z)}{r(x,y,z)}, \text{ where} \qquad (1)$$
$$r = \left(x^2 + y^2 + z^2\right)^{1/2}$$

and with the boundary conditions of disappearing pressure gradient on the walls in the direction of the normal vector and zero pressure at water surface, viz.

$$\frac{\partial p}{\partial \mathbf{n}} = 0 \text{ on the walls, where } \mathbf{n} \text{ is wall unit normal vector,} \qquad (2)$$
$$p = 0 \text{ on the water surface.}$$

The solution for the pressure by the MOI in the case of one point source can be obtained from

$$p(x,y,z) = \frac{S}{r(x,y,z)} + \sum_j \frac{S_j}{r_j(x,y,z)}, \text{ where} \qquad (3)$$

$S_j =$ source or sink strength for the j:th image source or sink (S or $-S$),

$r =$ distance from the real source,

$r_j =$ distance from the j:th image source or sink.

A FORTRAN77 program applying the MOI was written in order to perform the calculations for the subtask. The input of the program consists of

- number of mirrored pools to each direction,
- number of point sources (bubbles, or blowdown pipes),

- strength of each point source (N/m^3),
- co-ordinates for each point source (m),
- pool dimensions (m),
- co-ordinates of the points where the pressure is to be calculated (m).

The program calculates the pressure and partial derivatives of pressure to each direction in the points given in the input.

2.1.2 Numerical Model for the Water Pool

The POOLEX test facility was approximated with two different rectangular geometry pools as input to the MOI:

1. The equal volume approximation: the square shaped pool has the same volume of water as the original test rig, and also the horizontal intersection area is equal. The location of the point source (the end of the blowdown pipe) is chosen from the diagonal of the horizontal intersection such that the minimum distance to the wall is the same as within the POOLEX test rig.
2. The conservative approximation: the square shaped pool is the biggest one that fits into the original POOLEX cylindrical pool. The location of the point source is determined equally with the case 1.

The dimensions and other measures of the pools are as follows:

POOLEX test rig (Laine and Puustinen, 2003):
- water level 3.78 m from the centre point of the bottom,
- inner diameter 2.4 m,
- height of the bottom cone 0.454 m,
- location of the blowdown pipe end: 1 m up from bottom, 0.3 m horizontally from the centre z-axis.

The equal volume rectangular approximated pool:
- water level 3.48 m from the bottom,
- side length of the square profile 2.13 m,
- location of the blowdown pipe end: co-ordinates (0.9 m, 0.9 m, 1.0 m).

The conservative rectangular approximated pool:
- water level 3.33 m from the bottom,
- diameter of the square profile 2.4 m, side length 1.70 m,
- location of the blowdown pipe end: co-ordinates (0.9 m, 0.9 m, 1.0 m).

The point source strength is determined as: the extra pressure due to chugging at the locations of maximum estimated bubble radius is assumed to be equal to the hydrostatic head of water at that depth. This is assumed to be the scale for local pressure when the bubble has just collapsed and the water shock wave following the rarefaction wave has appeared. The time scale for such bubble collapsing is assumed to be 10 ... 100 ms, which leads to bubble interface velocity range of 1 ... 10 m/s, with the assumption of the maximum bubble radius being twice the blowdown pipe radius. This velocity is far smaller than the speed of sound in water, which justifies the assumption of incompressibility.

The number of mirrored pools has been chosen such that the desired convergence criteria are met (pressure normal gradient divided by pressure required to be less than 0.01 m^{-1} on the side walls and on the bottom), which was achieved with 35 reflections to each direction.

2.1.3 Numerical Results for the Pool

Figures 1 and 2 show the pressure caused by the point source (viz. the air pressure and the hydrostatic head are neglected to better visualise extra load due to the bubble collapsing) at different levels of the pool for both the equal volume and the conservative volume approximated pools. The extra pressure is at its maximum in the vicinity of the point source, which can clearly be seen from Figs. 1(*b*) and 2(*b*) describing the level at which the blowdown pipe end is located.

The extra pressure on one of the side-walls is presented in Figs. 3 and 4. The pressure varies between 0 and circa 14 kPa on the side-walls. This is coarsely in accordance with the findings in the POOLEX experiments of the extra pressure variation range due to chugging being about 5 kPa. In the MOI calculations, the wall pressure for the conservative pool approximation was slightly higher than for the equal volume approximated pool, as was expected.

The boundary conditions satisfaction level is visualised in Figs. 5 and 6. The normal pressure gradient normalised with the pressure has been plotted. It can be noticed from the scale of z-axis that numerical error in the boundary conditions is sufficiently small for the purpose of this study.

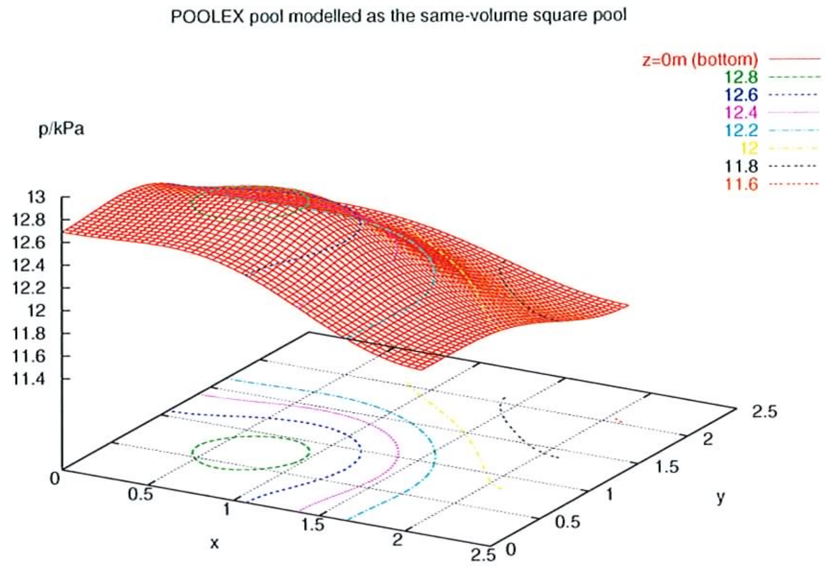

Figure 1(a). Pressure at the pool bottom for the equal volume square pool approximation.

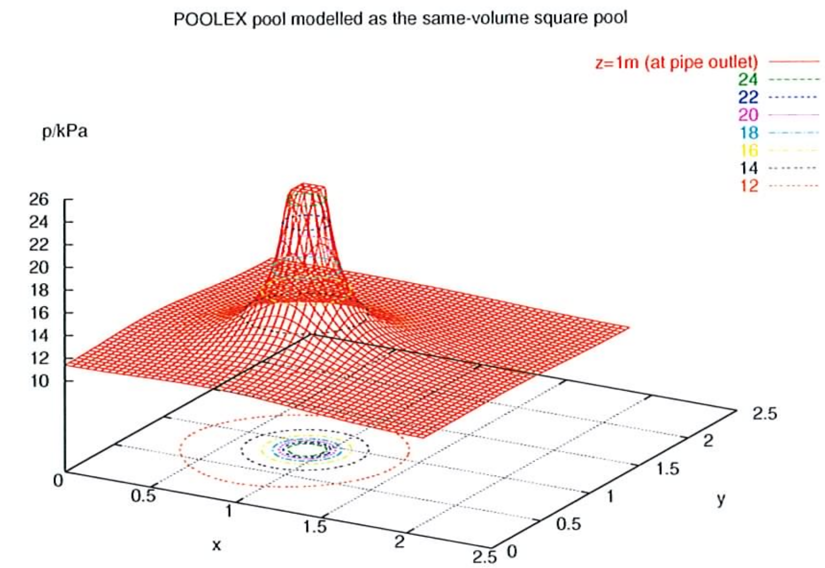

Figure 1(b). Pressure at 1 m level for the equal volume square pool approximation. The pressure has been cut within the volume of virtual maximum bubble because the model is not applicable there.

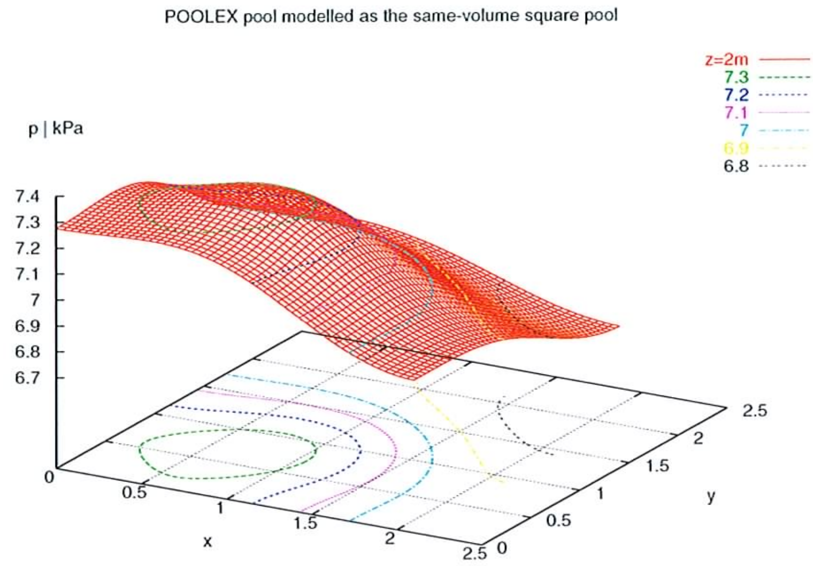

Figure 1(c). Pressure at 2 m level for the equal volume square pool approximation.

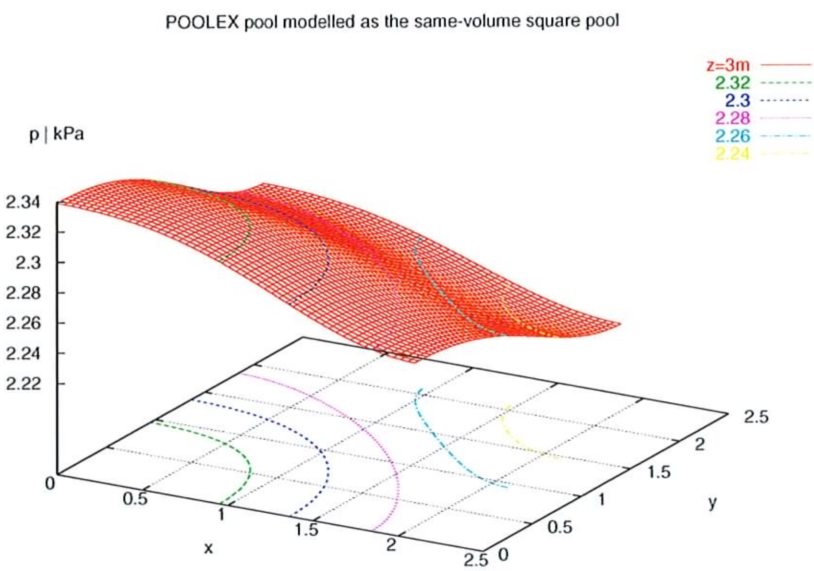

Figure 1(d). Pressure at 3 m level for the equal volume square pool approximation.

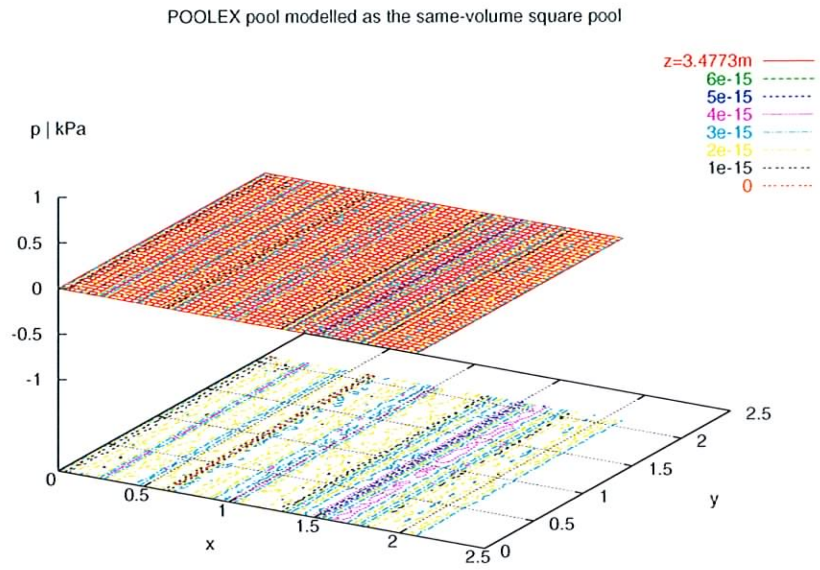

Figure 1(e). Pressure at 3.48 m level (at the water surface) for the equal volume square pool approximation.

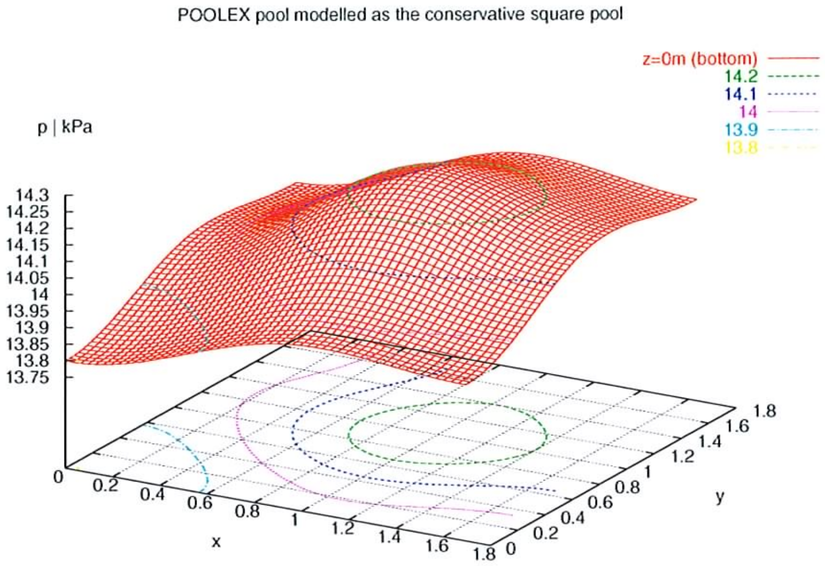

Figure 2(a). Pressure at the bottom of the pool for the conservative volume square pool approximation.

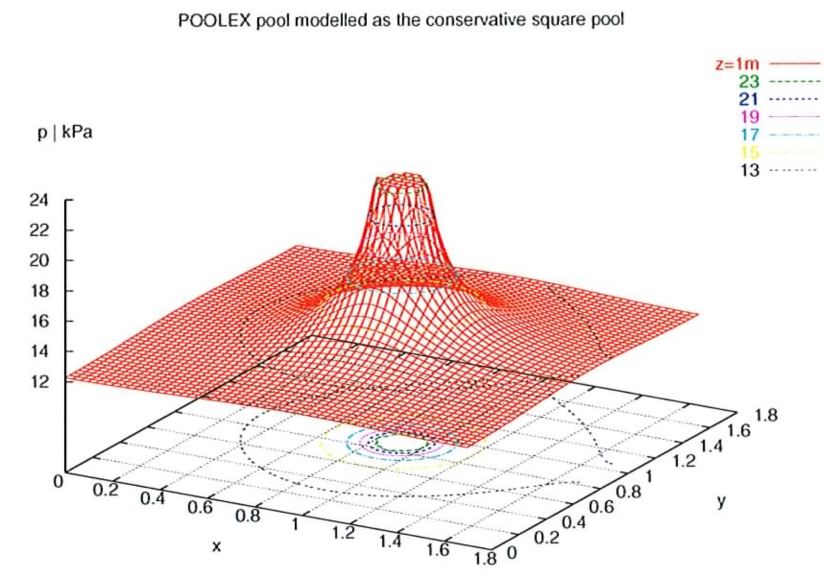

Figure 2(b). Pressure at the level 1 m for the conservative volume square pool approximation. The pressure has been cut within the volume of virtual maximum bubble because the model is not applicable there.

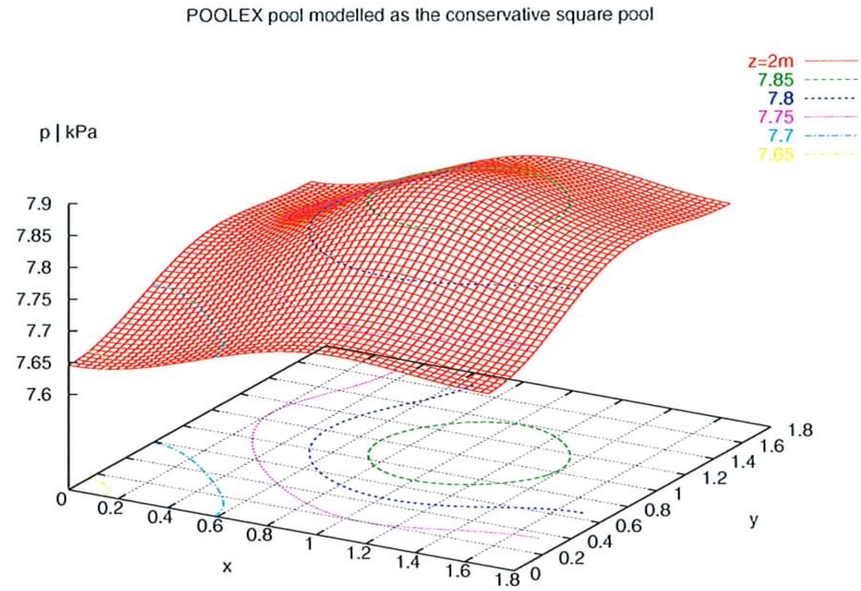

Figure 2(c). Pressure at the level 2 m for the conservative volume square pool approximation.

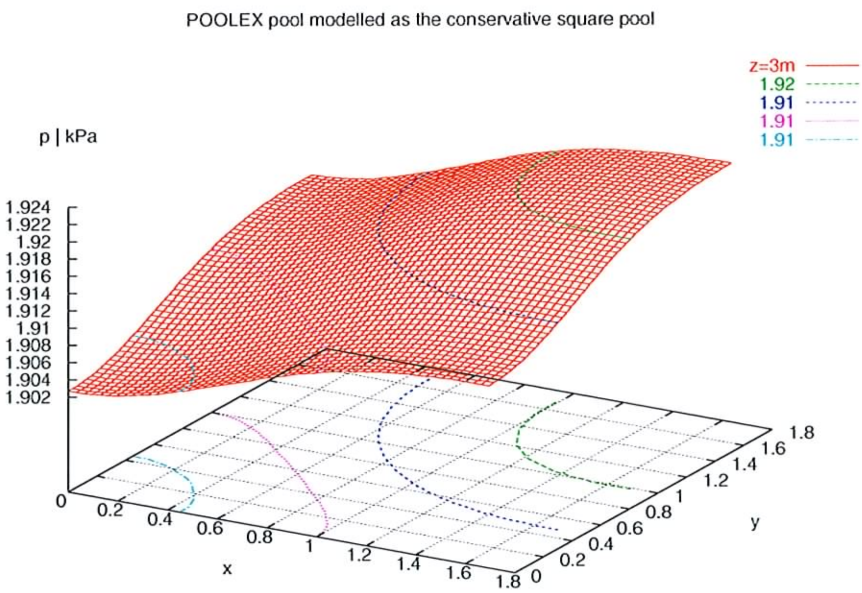

Figure 2(d). Pressure at the level 3 m for the conservative volume square pool approximation.

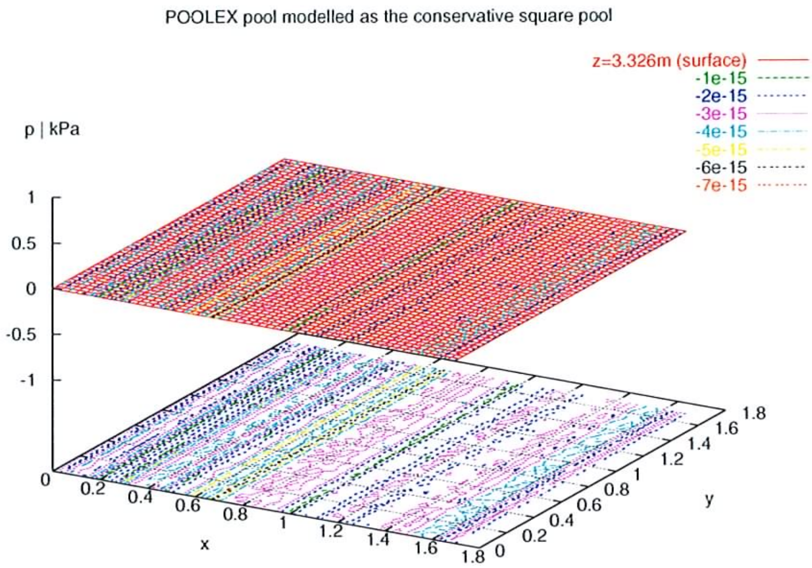

Figure 2(e). Pressure at the level 3.33 m (at the water surface) for the conservative volume square pool approximation.

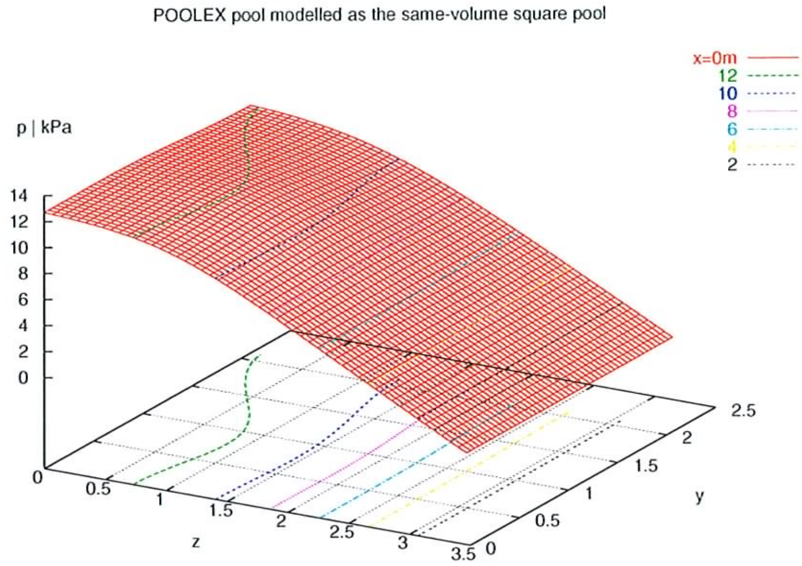

Figure 3. Pressure at the sidewall for the equal volume square pool approximation.

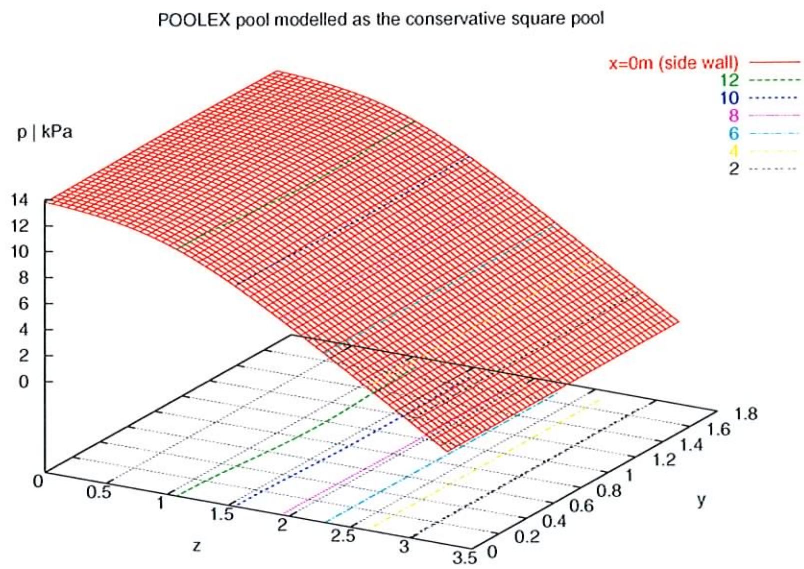

Figure 4. Pressure at the sidewall for the conservative volume square pool approximation.

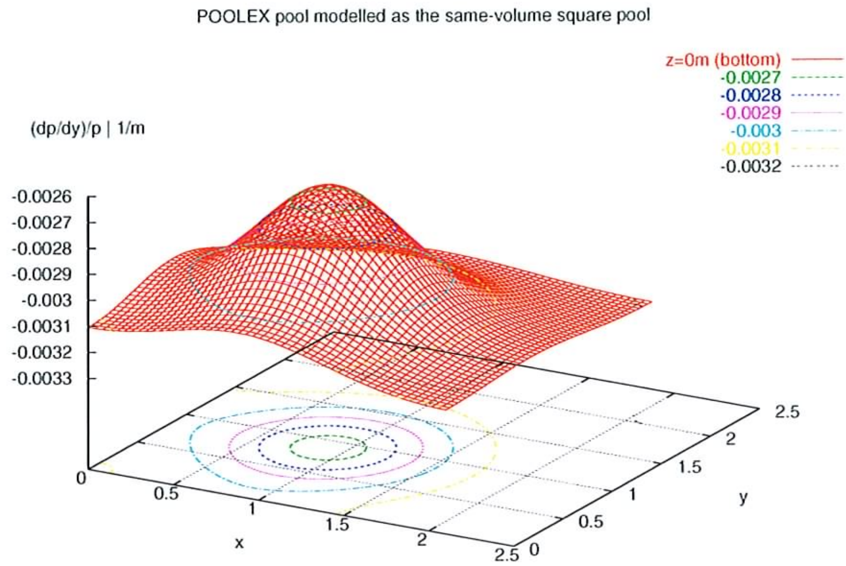

Figure 5(a). Normalized pressure normal gradient at the bottom of the pool for the equal volume square approximation.

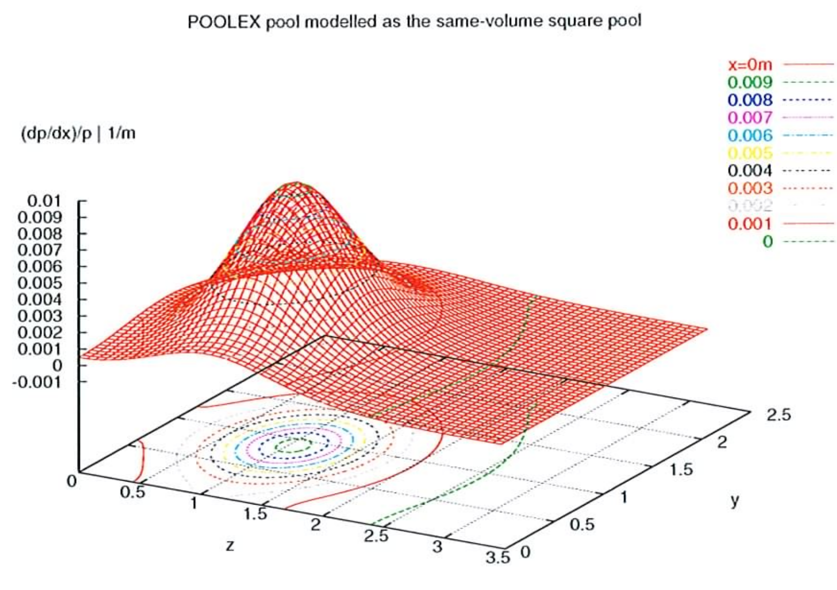

Figure 5(b). Normalized pressure normal gradient at the sidewall of the pool for the equal volume square approximation.

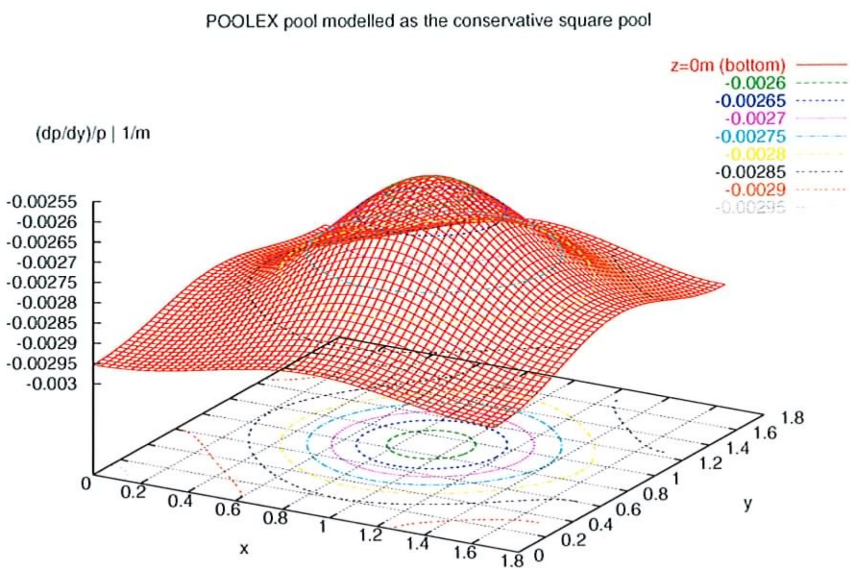

Figure 6(a). Normalized pressure normal gradient at the bottom of the pool for the conservative volume square approximation.

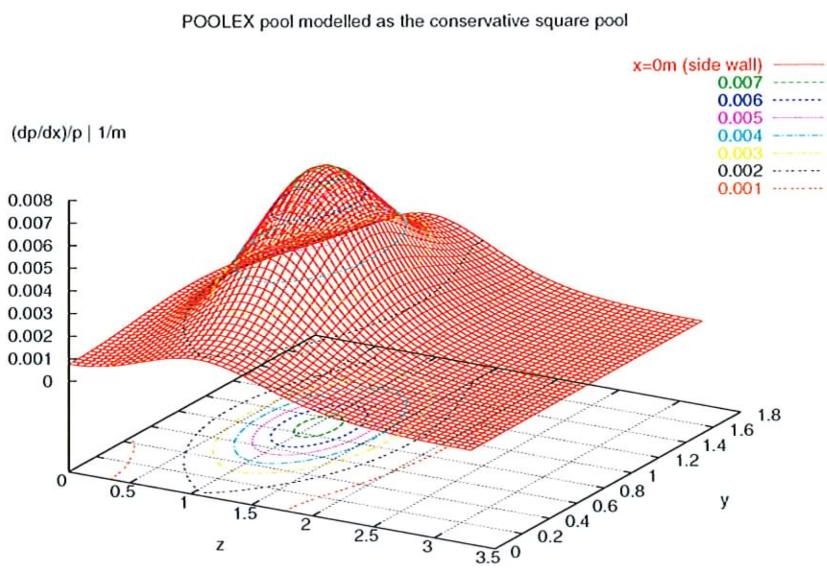

Figure 6(b). Normalized pressure normal gradient at the sidewall of the pool for the conservative volume square approximation.

2.1.4 Conclusions on the Method of Images

The Method Of Images (MOI) has been studied in order to estimate pressure loads to POOLEX test rig walls during gas discharge. The case considered here involves steam discharge such that the chugging phenomenon appears. Then the maximum bubble size and pressure when the bubble has collapsed has been estimated by heuristic reasoning. An independent bubble dynamics model, e.g. from the work of Giencke (1981), would have improved this step, but it was omitted at this stage because of schedule reasons. In the future, if this analysis is continued, it is necessary to use a model for bubble dynamics because of its central role in determining the point source strength for, and consequently the pressure field by the MOI.

The MOI is not directly applicable to the cylindrical (and conical at the bottom) geometry of the POOLEX test facility. Therefore, it has been simulated by two different approximations: the equal volume and conservative volume square pools. The equal volume approximated pool has the same area of intersection and the same total water volume as the original test rig. The conservative volume approximated pool represents the biggest rectangular pool to fit into the original test rig. The results for the conservative square pool should be regarded as the upper limit for the maximum wall pressure that is possible to achieve in the situation simulated.

The order of magnitude of pressure loads on the walls calculated by the MOI was within the range achieved with POOLEX pool measurements, viz. the extra pressure resulted from chugging was 5 – 10 kPa. The calculated pressures on the walls are systematically slightly higher for the conservative volume than for the equal volume square pool, as was expected.

The analysis should be refined in the future with the use of an independent bubble dynamics model. At current state, only heuristic reasoning for the maximum bubble radius and pressure was used. Therefore, these results should be considered as preliminary and only to give guidance about the range of real pressure loads during chugging.

This study showed that the MOI is a straightforward, yet suitable method for obtaining estimate for the wall loads in a BWR suppression pool during gas discharge or chugging. In the actual application to BWR, the geometry needs to be modified for the MOI because the suppression pool is typically of annular form. The modification can be performed by cutting the annulus and by describing the whole pool volume by a long rectangular pool (the horizontal length being the average circumference of the original annulus).

Other possible means worth studying to calculate the problem area, apart from a direct three-dimensional CFD simulation, would be to use the analytic solution for the Poisson equation, following the guidelines described in Wood et al. (1980) or to apply a suitable difference scheme to the problem viz. to solve it numerically as a steady-state three-dimensional flow problem or even as reduced to two-dimensional. These methods are to be considered in the future if still found suitable for the research program.

2.2 Homogeneous Two-phase Model for CFD Calculations

Homogeneous two-phase fluid model has been applied to simulate evaporation and condensation phenomena. In this fluid model, all material properties like void fraction density temperature viscosity etc. are defined as functions of fluid pressure and enthalpy. There is no transport equation for the void fraction because it is determined by pressure and enthalpy. This way all two-phase problematic matters have been included in the material property functions. In consequence, the CFD code has to solve just a single phase fluid flow problem.

However, the homogeneous two-phase fluid model has two difficult properties. Firstly, the temperature – enthalpy relation cannot be inverted in the two-phase region. This causes problems when standard enthalpy equation is in use because the enthalpy equation relies on the $h = c_pT$ relation. Secondly the fluid density can vary from pure steam (1 kg/m^3) to pure water (1000 kg/m^3) in the flow domain. This variation depends on pressure. It means that the momentum, continuity and energy equations depend strongly on pressure through density.

The Star-CD code has been used as the CFD platform. Earlier, the Fluent code has been used unsuccessfully in this problem setting. The Star-CD code offers a better basis for the modelling because it allows, unlike in the Fluent code, the density can depend on pressure.

2.2.1 Flow Field Solution

In the simulated system, density can vary temporally as well as spatially from pure steam to pure water. Density dependence on pressure is very strong in the two-phase region near the transition to water (Fig. 7, Fig. 8), i.e., in the region where boiling/condensation takes place. In Star-CD the compressibility can be modelled by defining density function and its derivative with respect to pressure.

One can assume that this dependency has been modelled properly and works well when applied to single phase fluid. The pure water and steam each have roughly linear density functions and the density derivative is small ($10^{-6}/10^{-3}$). The very strong nonlinear nature of the dependence here may cause convergence problems.

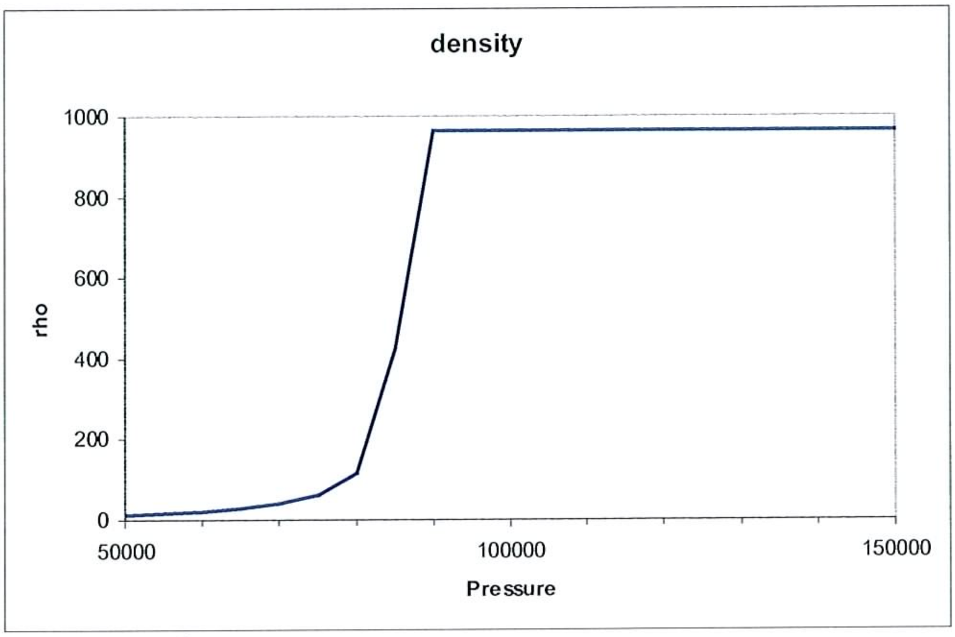

Figure 7. Density (kg/m^3) as function of pressure (Pa), constant enthalpy 400 kJ/kg.

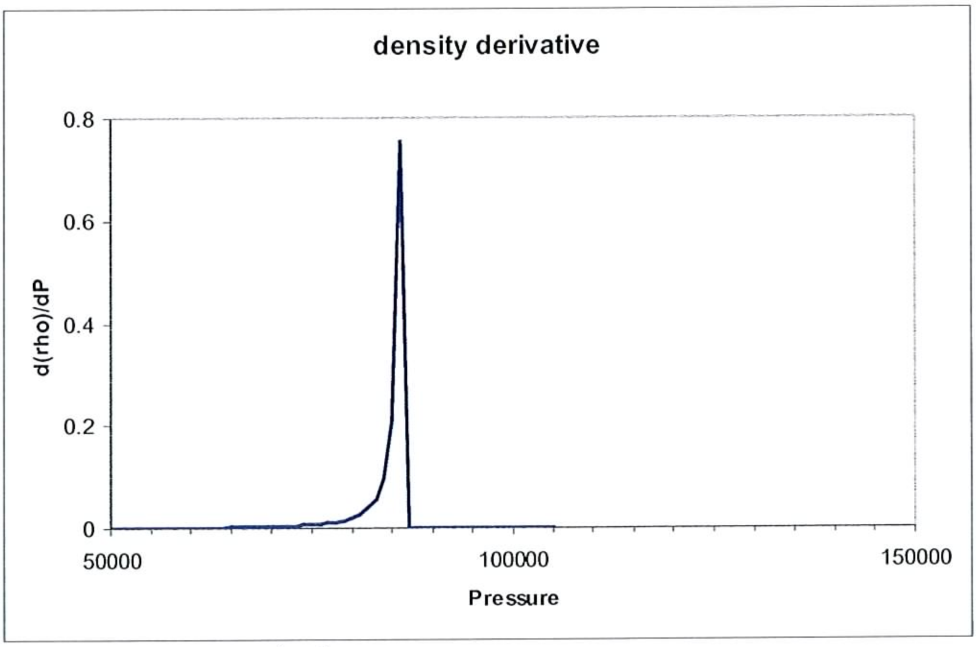

Figure 8. Density derivative (s^2/m^2) with respect to pressure (Pa), constant enthalpy 400 kJ/kg.

Using simplified mass and momentum balance equations the nonlinearity problems will be demonstrated in a single cell case.

$$\frac{\partial \rho}{\partial t} + \frac{\partial \rho u_j}{\partial x_j} = 0 \tag{4}$$

$$\frac{\partial \rho u_i}{\partial t} + \frac{\partial \rho u_j u_i}{\partial x_j} = -\frac{\partial p}{\partial x_i} + s_i \tag{5}$$

Integrating equation (4) over a control volume the mass balance can be expressed as follows

$$mass^{new} = mass^{old} - dt \bullet (flow\_rate\_out - flow\_rate\_in)$$

where the flow rates are computed using velocities from equation (5) (s_I=0).
The pressure solution can now be formulated as to find pressure p that satisfies the equation :

$$mass^{new}(p) = mass^{old} + dt \cdot flow(p)$$

It can be seen that when time step is small the new mass term dominates the equation whereas the flow term is determining term when time step is large. In Figs 9-11 the mass and flow terms have been depicted. The density function that dominates the solution when small time steps are used causes problems because its derivative is practically discontinuous.

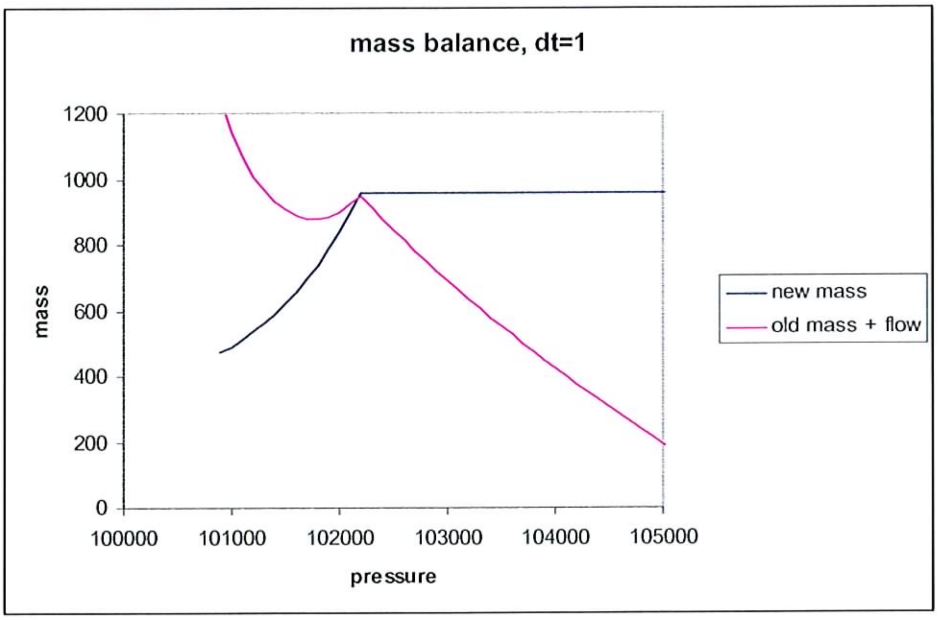

Figure 9. Mass (kg) versus pressure (Pa) balance equation, time step 1.0 s.

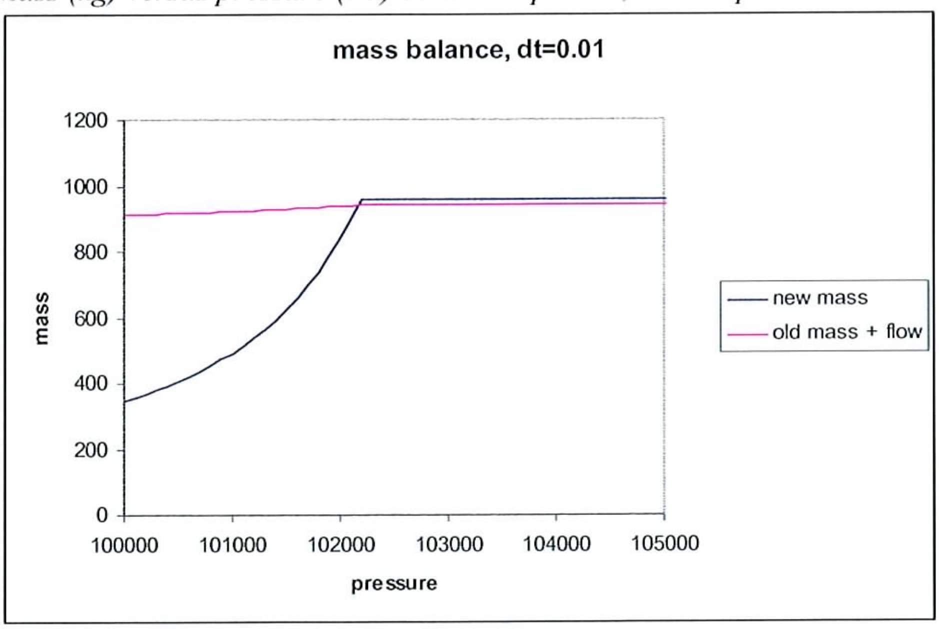

Figure 10. Mass (kg) versus pressure (Pa) balance equation, time step 0.01 s.

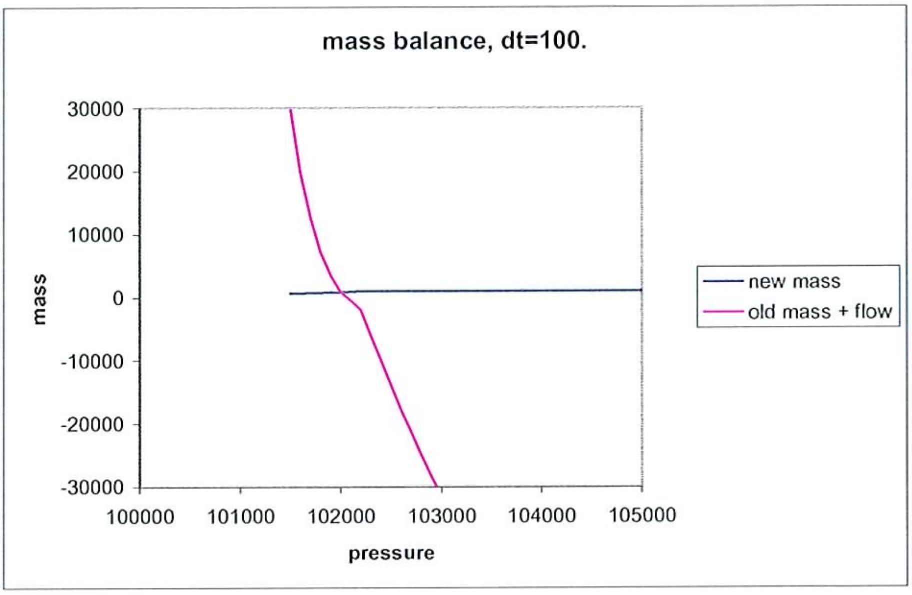

Figure 11. Mass (kg) versus pressure (Pa) balance equation, time step 100 s.

The test runs showed that the steady state simulation works well when SIMPLE algorithm was in use. That is, the flow dominated problem depicted in Figure 11 did converge. However the transient calculations failed to converge. Experience gained with APROS homogeneous two-phase model indicates that the density derivative should be replaced with computational derivative which is adjusted during iteration. Unfortunately, in the PISO algorithm which is obligatory in Star-CD transient calculations the algebraic equations corresponding equations (4) and (5) are evaluated only once per time step. It means that density and its derivative are updated only once in the time step thus it is not possible to adjust the density derivative. A smoothed density derivative was tested (Fig. 12) but it failed to improve convergence.

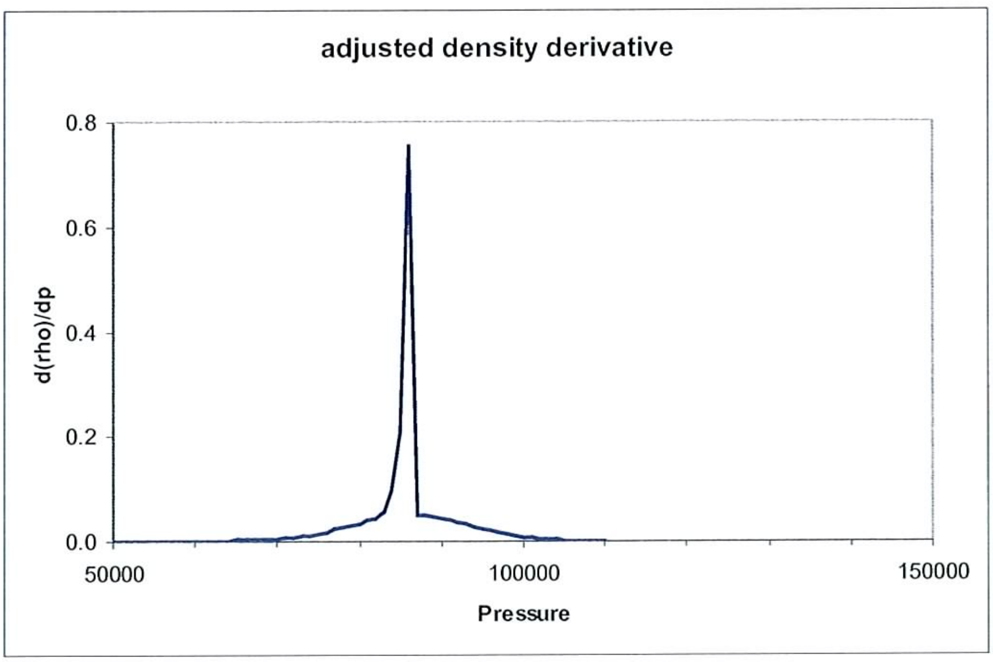

Figure 12. A smoothed density derivative (s^2/m^2) with respect to pressure (Pa).

2.2.2 Heat Transfer Solution

When turbulence model is in use, the STAR-CD enthalpy equation can be written as follows

$$\frac{\partial \rho h}{\partial t} + \frac{\partial(\rho u_j h - F_{h,j})}{\partial x_j} = S \qquad (6)$$

$$F_{h,j} = k\frac{\partial T}{\partial x_j} + \frac{\mu_t}{\Pr}\frac{\partial h}{\partial x_j} \qquad (7)$$

$$h = \overline{c_p}T - c_p^0 T_0 \qquad (8)$$

Equation (8) indicates that the temperature–enthalpy relation is invertible. In the homogeneous two-phase model this is not the case (Fig 13).

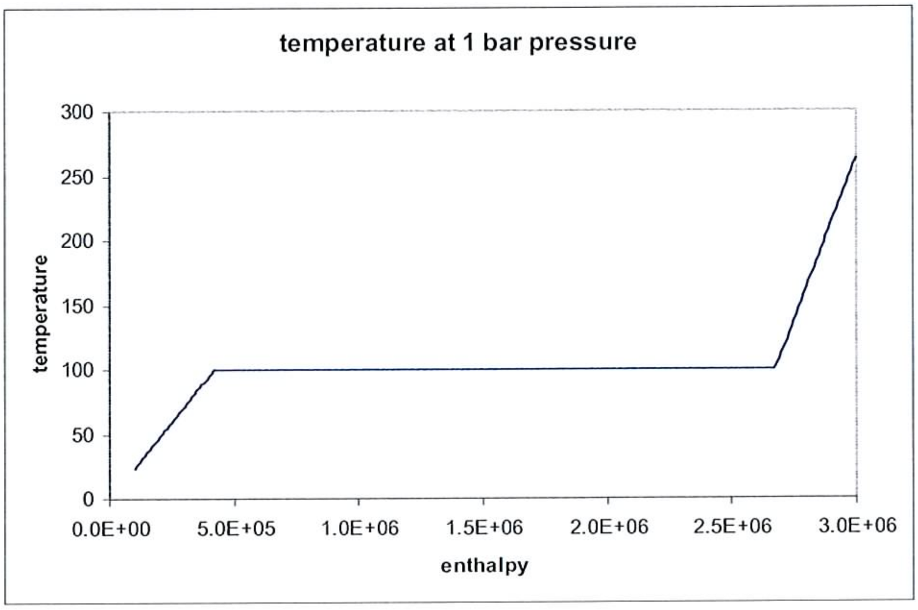

Figure 13. Non-invertible temperature(C)-enthalpy(J/kg) relation.

Another problem with the Star-CD enthalpy equation is that only temperature is accessible to the user defined subroutines. In the homogeneous two-phase model, it is necessary to know enthalpy because all material properties have been defined as functions of pressure and enthalpy.

Both problems can be circumvented by using a user-defined scalar transport equation.

$$\frac{\partial \rho h}{\partial t} + \frac{\partial(\rho u_j h - F_{h,j})}{\partial x_j} = S \qquad (9)$$

$$F_{h,j} = \frac{k}{c_{eff}}\frac{\partial h}{\partial x_j} \qquad (10)$$

$$c_{eff} = Xc_{p,steam} + (1 - X)\cdot c_{p,water} \qquad (11)$$

Here the coefficient of the enthalpy gradient should be examined closer. The drawback of the user defined enthalpy equation is that it cannot be connected to wall heat conduction solution.

Wall Heat Transfer

The heat flux and wall heat transfer coefficient are for start described using correlations found in the pipe flow documentary. They should be improved for 3d calculations when simulation experiences are gained.

The condensation model is (RELAP5, 1980)

$$q = h \cdot (T_{wall} - T_{sat})$$
$$h = \max(h_{lam}, h_{turb})$$
$$h_{lam} = 3.82332 \cdot 0.296 \left[\frac{\rho_f (\rho_f - \rho_g) \cdot g \cdot h_{fg} \cdot k_f^3}{D_e \mu_f (T_{sat} - T_{wall})} \right]^{0.25}$$
$$h_{turb} = 0.065 \frac{k_f \sqrt{\rho_f}}{\mu_f} \sqrt{\frac{\mu_f C_{p,f}}{k_f}} \sqrt{\frac{0.023 \mu_g |v_g|}{D_e}}$$

The condensation model is applied when Quality $X \geq 0$ and $T_{wall} \leq T_{sat}$. The Chen correlations have been applied to describe boiling (RELAP5, 1980; TRAC-M, 2000):

$$q = h \cdot (T_{wall} - T_{sat})$$
$$h = h_{mic} + h_{mac}$$
$$h_{mic} = 0.00122 \frac{k_f^{0.79} C_{p,f}^{0.45} \rho_f^{0.49}}{\sigma^{0.5} \mu_f^{0.29} h_{fg}^{0.24} \rho_g^{0.24}} (T_{wall} - T_{sat})^{0.24} p_{mic}^{0.75} \cdot S$$
$$h_{mac} = 0.023 \frac{k_f}{D_e} \Pr_f^{0.4} \mathrm{Re}_f^{0.8} \cdot F$$
$$F = 1, \text{ when } X_{TT}^{-1} \leq 0.1$$
$$F = 2.35 \left(X_{TT}^{-1} + 0.213 \right)^{0.736} \text{ when } X_{TT}^{-1} > 0.1$$
$$X_{TT}^{-1} = \left(\frac{x}{1-x} \right)^{0.9} \left(\frac{\rho_f}{\rho_g} \right)^{0.5} \left(\frac{\mu_g}{\mu_f} \right)^{0.1}$$
$$S = \left(1 + 0.12 \mathrm{Re}_{Tp}^{1.14} \right)^{-1} \text{ for } \mathrm{Re}_{Tp} < 32.5$$
$$S = \left(1 + 0.42 \cdot \mathrm{Re}_{Tp}^{0.78} \right)^{-1} \text{ for } 32.5 \leq \mathrm{Re}_{Tp} \leq 70.0$$
$$\mathrm{Re}_{Tp} = MIN(70.0, 10^{-4} \cdot (1-x) \mathrm{Re}_f \cdot F^{1.25})$$
$$p_{mic} = p_{sat}(T_{wall}) - p_{sat}(T_f)$$

The Chen correlation is used when Quality $X < 1$ and $T_{wall} \geq T_{sat}$. In other cases the Dittus-Boelter correlation is applied (RELAP5, 1980; TRAC-M, 2000):

$$q = h(T_{wall} - T)$$
$$h = 0.023 \frac{k}{D_e} \Pr^{0.4} \mathrm{Re}^{0.8}$$

2.2.3 Program Implementation

The homogeneous two-phase model has been implemented using user defined functions. All material properties of the steam/water mixture are defined in the steam table program STMPH. Density and molecular viscosity of the fluid are accessed by STAR-CD via subroutines DENSIT and VISMOL. In the user defined enthalpy transport equation, the diffusion term is defined in subroutine DIFFUS. The wall heat transfer is defined in the subroutine BCDEFW. Additional scalars like void fraction and temperature are defined in the subroutine SCALFN which gets the values from STMPH subroutine.

STAR-CD connections:

Thermophysical Models and Properties -> Liquids and Gases -> Molecular Properties -> Density = DENSIT
Thermophysical Models and Properties -> Liquids and Gases -> Molecular Properties -> Viscosity = VISMOL
Thermophysical Models and Properties -> Liquids -> Additional scalars -> Binary Properties -> Diffusivity = DIFFUS
Define Boundary Conditions -> Define Boundary Regions -> Wall -> User defined coding = BCDEFW
Analysis Controls -> Solution controls -> Equation Behavior -> Additional scalars -> Solution method = SCALFN

2.2.4 Simulations

As noted in describing the pressure solution the transient simulation failed so that only two steady state simulations are presented.

Steam Blowdown

A system where superheated steam in steel pipe enters a vessel filled with cold water was simulated. The system represents the Pactel test facility and the experiments carried out there. Figures 14 and 15 show the results.

System characteristics are:

- steam flow 0.4 kg/s, T = 162 C (T_sat =133 C), p = 1.3 bar
- water temperature 28 C
- pipe inner wall T = 100 C, outer wall T=85 C, calculated separately, no conjugate heat transfer in use

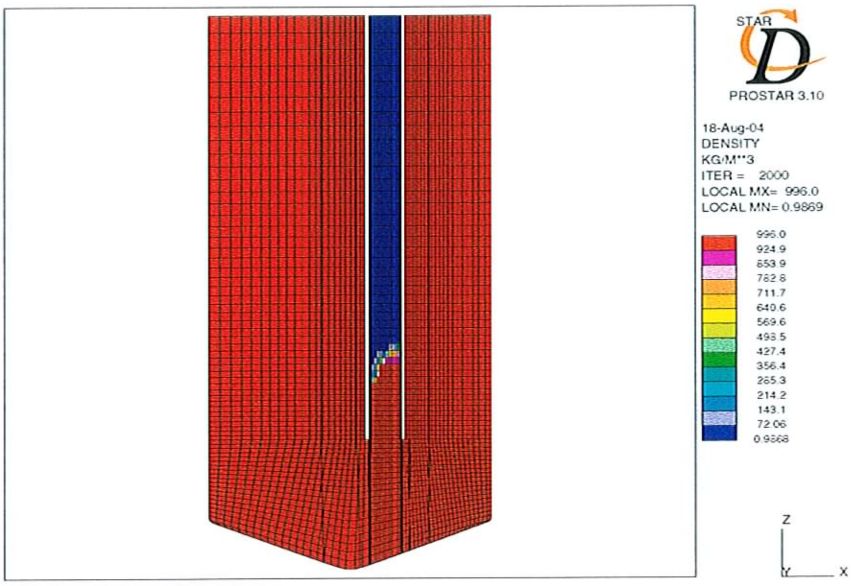

Figure 14. Density field.

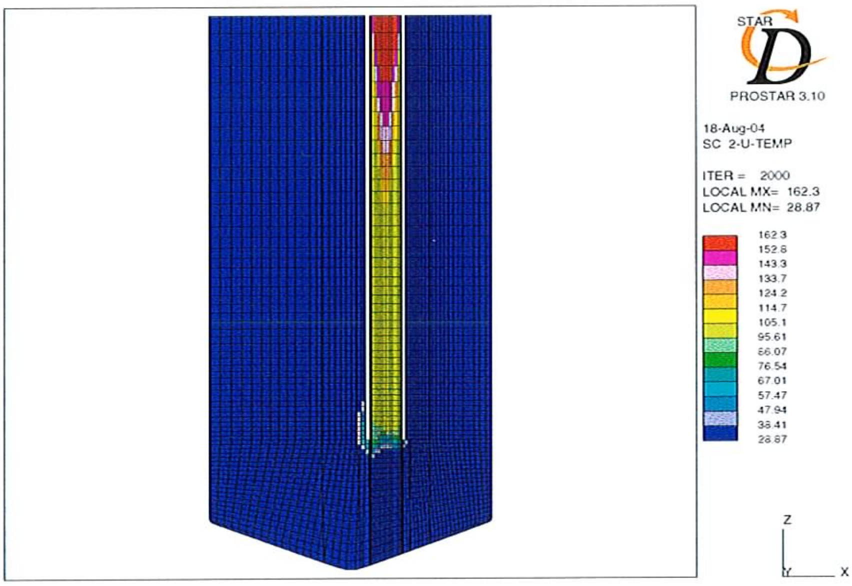

Figure 15. Temperature distribution.

Although comparing measured data of a transient to steady-state simulation data is not quite adequate it could reveal the severe errors of the simulation model. Here the pressure and temperature fields agree quite well with measurements. Also the water level in the pipe agrees well with the measurements.

Steam Flow in a Bended Pipe

Related to the preceding case the steam flow in a bended pipe was simulated.

The system characteristics are:

- Superheated steam in pipe where horizontal section is adiabatic and vertical section is cooled
- steam mass flow 0.24 kg/s, T = 163 C, p =1.3 bar
- cooled wall T= 28 C

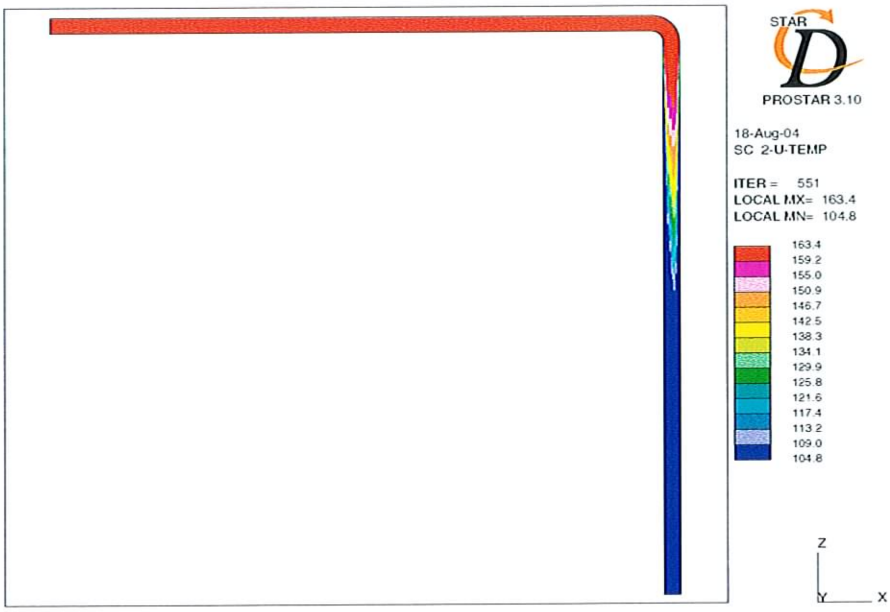

Figure 16. Temperature in the bended pipe.

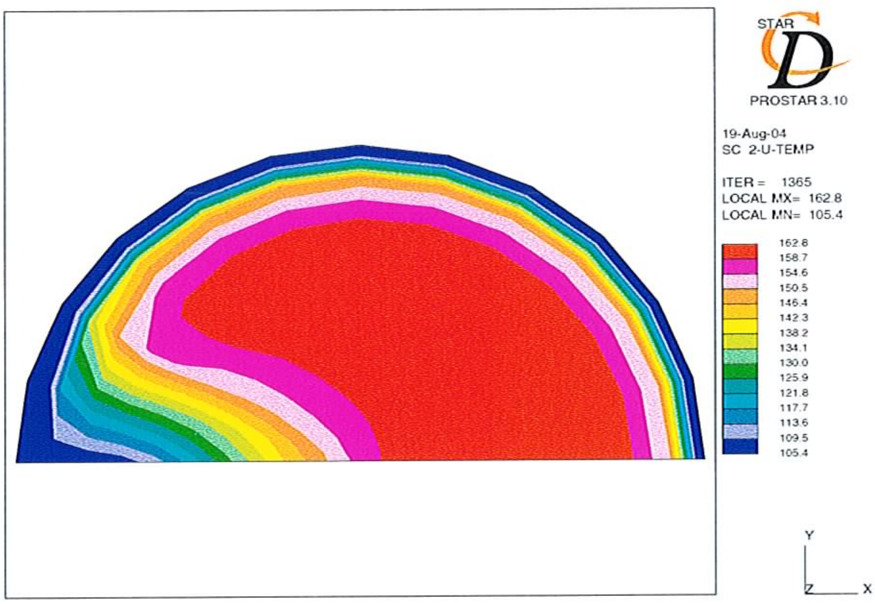

Figure 17. Temperature cross-section at vertical pipe near the bending.

2.3 Analytical Model for Rapid Condensation of a Bubble

In the FSI simulations of Sec. 3.5, rapid collapse of a bubble is modelled with a simple analytical model used previously in the simulations, where rigid pool wall was assumed. The model is based on the potential theory of an incompressible fluid. The spherical steam region has initially a radius R_0 in an infinite region of water with a density ρ. The pressure difference causing the collapse is assumed to be constant: $\Delta p_B = p_0 - p_B$, where p_0 is the pressure far away from the bubble and p_B is pressure on the bubble surface.

The equation of motion for the surface of the bubble is integrated by using the potential of the flow velocity. It is found that the bubble surface collapses with the velocity

$$\dot{R}(t) = -\left(\frac{2\Delta p_B}{3\rho}\right)^{1/2}\left(\frac{R_0^3}{R(t)^3}-1\right)^{1/2}, \qquad (12)$$

where $R(t)$ is the radius of the bubble at time t and $\dot{R}$ stands for the time derivative.

The mass flux at the surface of the bubble is

$$\dot{m}(t) = -4\pi\left(\frac{2}{3}\Delta p_B \rho\right)^{1/2} R(t)^{1/2}\left(R_0^3 - R(t)^3\right)^{1/2}. \qquad (13)$$

The bubble has initially a radius of $R_0 = 10$ cm is considered. The radius collapses to the value zero within a time of $t_{tot} \approx 25$ ms.

In Sec. 3.5, a rapid condensation of a steam bubble is modelled with a single-phase calculation by applying the mass sink of Equation (13) into the water pool. The pressure transient caused by the collapsing bubble consists of two different stages (Giencke, 1981). The early phase of the collapse consists of a fairly long period of under pressure, which pushes water into the region of the bubble. At the end of the collapse, a rapid over pressure occurs because water flowing into the centre of the bubble is stopped rapidly when the bubble is filled.

A more detailed description of the model can be found in Timperi et al. (2004).

3 Fluid-structure Interaction Analysis of the Pool

ES-FSI uses a method in which the deformations of the structure are solved during the CFD calculation without the need of simultaneous coupling of CFD and FE codes. Star-CD version 3.15A (Anon., 2001) is used for the flow calculations. The structural analyses are conducted with ABAQUS/Standard version 6.4.1 (ABAQUS, 2003a).

Solving an FSI problem with ES-FSI can be divided into three steps: pre-analysis of the structure, FSI analysis and post-analysis of the structure. These three steps are discussed shortly in the following section. Analysis with ES-FSI includes substructuring of the FE model, substructures and substructure analysis are discussed in Sec. 3.2. The FE model of the pool is presented in Sec. 3.3. The pre-analysis of the pool structures, FSI analysis and post-analysis of the pool are presented in Secs. 3.4, 3.5 and 3.6, respectively.

3.1 FSI Calculation with ES-FSI

In the pre-analysis of the structure, degrees of freedom (DOF) of the FE model lying at the fluid-structure interface, and possibly certain other DOF, are selected as master degrees of freedom (MDOF). A substructure of the original FE model is generated by using the selected set of MDOF. The substructure analysis produces reduced stiffness and mass matrices for the substructure. The reduced structural model matrices, which relate only the MDOF, are used to solve the motion of the structure during the FSI analysis. ABAQUS writes the reduced matrices into a text file, which is read by ES-FSI at the beginning of the FSI analysis.

The FSI analysis consists of a standard Star-CD transient moving mesh analysis, which is run with ES-FSI. The reduced structural model matrices are used by ES-FSI to solve the motion of the structure. The near-wall mesh is moved with the aid of the Pro-Star pre-processor macro or by using a user-defined Fortran routine.

The retained nodes on the substructure can form triangular or quadrilateral patches for the interpolation. The fluid cell pressures are interpolated on the structural model and the equivalent nodal forces on the retained nodes are calculated. Linear FE shape functions are used to calculate the displacements of the CFD mesh surface vertices from the displacements of the MDOF. The implicit Newmark method is used for direct-integration of the structure. The Newmark method results to an effective structural model matrix, which is constant with fixed time step size. The matrix is inverted by ES-FSI only once at the beginning of the analysis. This results to a relatively small additional cost of solving the motion of the structure.

In the post-analysis of the structure, the displacements of the MDOF through time, written by ES-FSI into a text file, are read into ABAQUS. The solution internal to the substructure is recovered, i.e., the resulting displacements and stresses throughout the original FE model can be post-processed.

3.2 Substructure Analysis

A substructure is a group of elements from which all but the MDOF have been eliminated on the basis of linear behaviour of the group. The eliminated DOF are termed slave degrees of freedom (SDOF). The response of a substructure is defined by reduced stiffness, mass and damping matrices, which contain only elements corresponding to the MDOF. A substructure appears in FE analysis only through the MDOF, at retained nodes, for which loads or boundary conditions can be applied. A restriction is that the response of a substructure is fully linear. Substructures are described more closely in ABAQUS (2003a) and Cook et al. (2002).

3.2.1 Condensed Matrices

The condensed stiffness matrix for a subtructure is obtained by the Guyan reduction. Below we follow the representation in ABAQUS (2003a). The contribution of the substructure to the virtual work of the model can be written as

$$\delta W = [\delta u^{M} \quad \delta u^{S}]\left(\begin{Bmatrix} \Delta P^{M} \\ \Delta P^{S} \end{Bmatrix} - \begin{bmatrix} K^{MM} & K^{MS} \\ K^{SM} & K^{SS} \end{bmatrix}\begin{Bmatrix} \Delta u^{M} \\ \Delta u^{S} \end{Bmatrix}\right), \tag{14}$$

where $\{\delta u\}$ are virtual displacements, $\{\Delta P\}$ are nodal forces, $\{\Delta u\}$ are displacements, $[K]$ is the tangent stiffness matrix and letters M and S in the superscripts refer to master and slave degrees of freedom, respectively. The equilibrium equations related to the virtual displacements of the SDOF in Equation (14) are complete within the substructure, since the SDOF appear only within the substructure:

$$\{\Delta P^{S}\} - [K^{SM}]\{\Delta u^{M}\} - [K^{SS}]\{\Delta u^{S}\} = 0, \tag{15}$$

or

$$\{\Delta u^{S}\} = [K^{SS}]^{-1}(\{\Delta P^{S}\} - [K^{SM}]\{\Delta u^{M}\}). \tag{16}$$

Substitution of Eq. (16) into Eq. (14) gives

$$\begin{aligned} \delta W = [\delta u^{M}](\{\Delta P^{M}\} - [K^{MS}][K^{SS}]^{-1}\{\Delta P^{S}\} - \\ ([K^{MM}] - [K^{MS}][K^{SS}]^{-1}[K^{SM}])\{\Delta u^{M}\}) \end{aligned}. \tag{17}$$

The reduced stiffness matrix is then

$$[\overline{K}] = [K^{MM}] - [K^{MS}][K^{SS}]^{-1}[K^{SM}]. \tag{18}$$

Reduced mass and damping matrices for a substructure are obtained with the same transformation as in Eq. (18). It is important to notice however, that use of the reduced matrices in dynamic analyses introduces approximations to the analyses, contrary to a static case. This is discussed shortly in the next section.

It may be noted here, that in ABAQUS only the reduced stiffness and mass matrices can be generated. For direct-integration dynamic analysis, Rayleigh damping can be included for a substructure by defining the mass and stiffness proportional damping parameters. In ES-FSI, the Rayleigh damping parameters are defined in the ES-FSI input file when material damping for a substructure is included in the analysis.

The reduced matrices of a substructure are fully populated, i.e., they have no zero elements, even if the original matrices are diagonal or sparse (Cook et al., 2002). In normal FE analyses, sparse and banded matrices are usually obtained. Accordingly, memory requirement needed to generate the reduced matrices for a substructure can be very large compared to analyses with the original FE model, if the number of MDOF is large. This is discussed later in Section 3.4.1.

3.2.2 Substructures in Dynamic Analyses

In linear static analyses, no approximations to the response of the model are made when a substructure is used. However in dynamic analyses, approximations are introduced by the fact that dynamic modes within the structure can only be represented by degrees of freedom inside the structure, which are usually condensed out either partly or entirely as SDOF. The substructure may not then be accurate, if the dynamic modes are important. Accuracy of the dynamic response can be improved by retaining additional DOF inside the substructure. (Cook et al., 2002; ABAQUS, 2003b)

The selected MDOF should have a large mass-to-stiffness ratio to obtain high accuracy in dynamic analyses, i.e., either elements in $[K^{MM}]$ in Equation (14) should be small or elements in the corresponding mass matrix $[M^{MM}]$ should be large. This is because the stiffness matrix of the original structure alone dictates how the SDOF will follow the motion of the MDOF. Accordingly, rotational DOF are rarely retained to improve accuracy in dynamic analyses (Cook et al., 2002). An automated choice of the MDOF for dynamic analyses is described in Cook et al. (2002). In the method, mass-to-stiffness ratio for DOF is scanned and the desired number of SDOF is eliminated on the basis of the ratio. It should be noted that in the analyses with ES-FSI, it may usually be necessary to retain also DOF with a small mass-to-stiffness ratio, i.e., non-optimal DOF in the sense of structural dynamics. This is due to accuracy requirements of interpolating the coupling quantities and representing deformations of the structure, as discussed in sections 3.6 and 4.

3.3 FE Model of the Pool

A three-dimensional FE model with different element types is used for the structural analyses. The geometry of the model corresponds relatively accurately to the real pool and its supporting structures. The model is the same as used earlier in the one-directional FSI analysis of the pool (Timperi et al., 2004).

The pool itself and L-profile stiffening upper edge of the pool are stainless steel SS2333, U-profile bracings around the pool are normal steel S235JRG2 and rectangular support beams are normal steel S355J2H. Material properties used in the FE model are listed in Table 1. An elastic-plastic material model was used in the earlier analyses of the pool (Calonius et al., 2003; Timperi et al., 2004). In this work however, a substructure of the FE model is used in the FSI calculation. Therefore, the model has fully linear behaviour and only the elastic material properties are used.

Table 1. Elastic material properties and density used in the FE analyses.

SS2333			S235JRG2			S355J2H		
E [GPa]	ν	ρ [kg/m^3]	E [GPa]	ν	ρ [kg/m^3]	E [GPa]	ν	ρ [kg/m^3]
206	0.3	7900	206	0.3	7850	206	0.3	7850

The pool is meshed with 4-node shell elements, triangular 3-node shell elements are used in some few necessary locations. The size of the elements is at most part of the model approximately 100 × 100 mm. The beams are meshed with 2-node linear beam elements. The length of the beam elements is at most part 100 mm. The number of elements in the whole model is 6585 and the number of nodes is 7310. The pool mesh and a detailed picture of the pool bottom mesh are shown in Figure 18.

The disc springs under the vertical supports were modelled with nonlinear springs in the earlier studies. In this work due to substructuring, the springs are modelled as linear according to their initial stiffness. The initial stiffness of the disc springs is approximately 42 MN/m. The FE model is presented in more detail in Timperi et al. (2004).

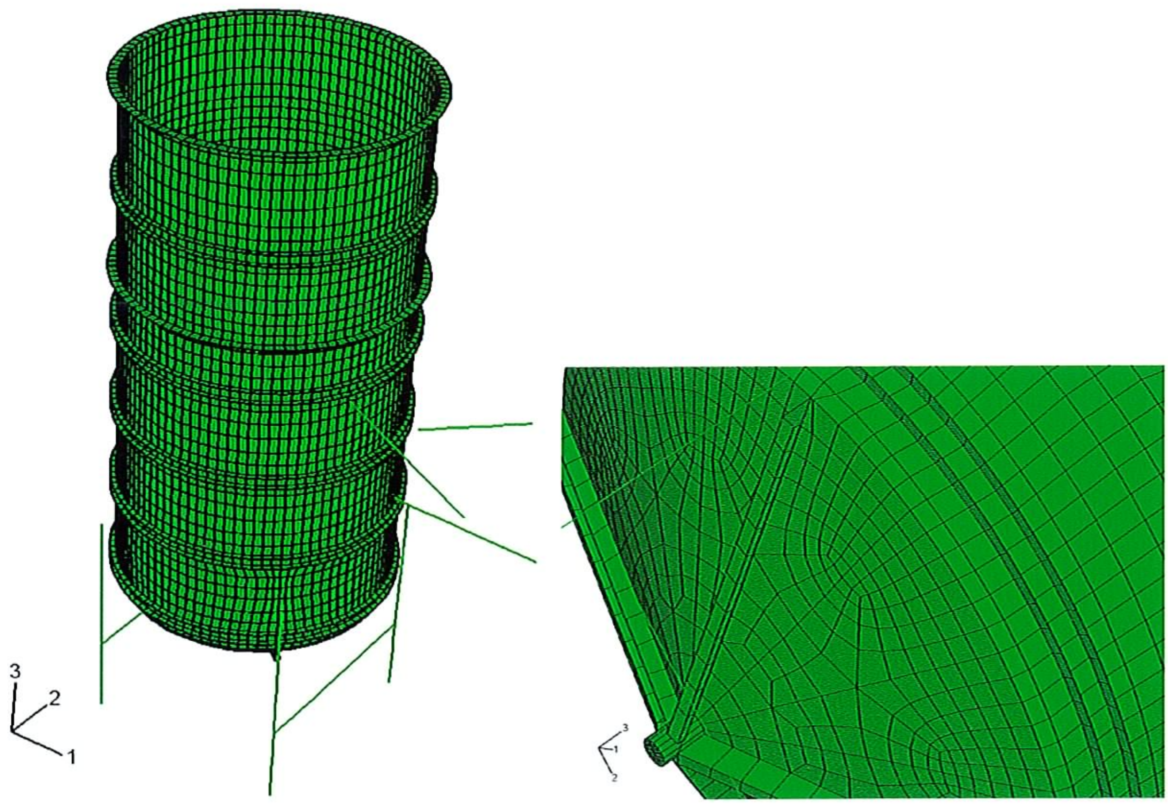

Figure 18. The pool mesh and the supports. On the right: a detail of the pool bottom mesh.

3.4 Pre-analysis of the Pool Structures

Substructure analyses with different selections of MDOF are performed for the pool to examine the effect of the choice of MDOF on computational cost and accuracy of the substructures. Memory requirement and analysis time of different analyses are examined. Accuracy obtained in dynamic analyses with different choices of MDOF is examined by comparing eigenmodes of selected substructures to the corresponding eigenmodes of the original FE model.

Retained nodes in the different selections of MDOF are shown in Figure 19. Different substructures of the FE model of the pool are listed in Table 2. Retained nodes and DOF and the resulting number of MDOF for the different substructures are presented in Table 2. In the case of Substructure 6, all unconstrained nodes on the fluid-structure interface, i.e., 5059 nodes, are retained. Substructure 3 in Table 2 is used in the FSI analysis with ES-FSI.

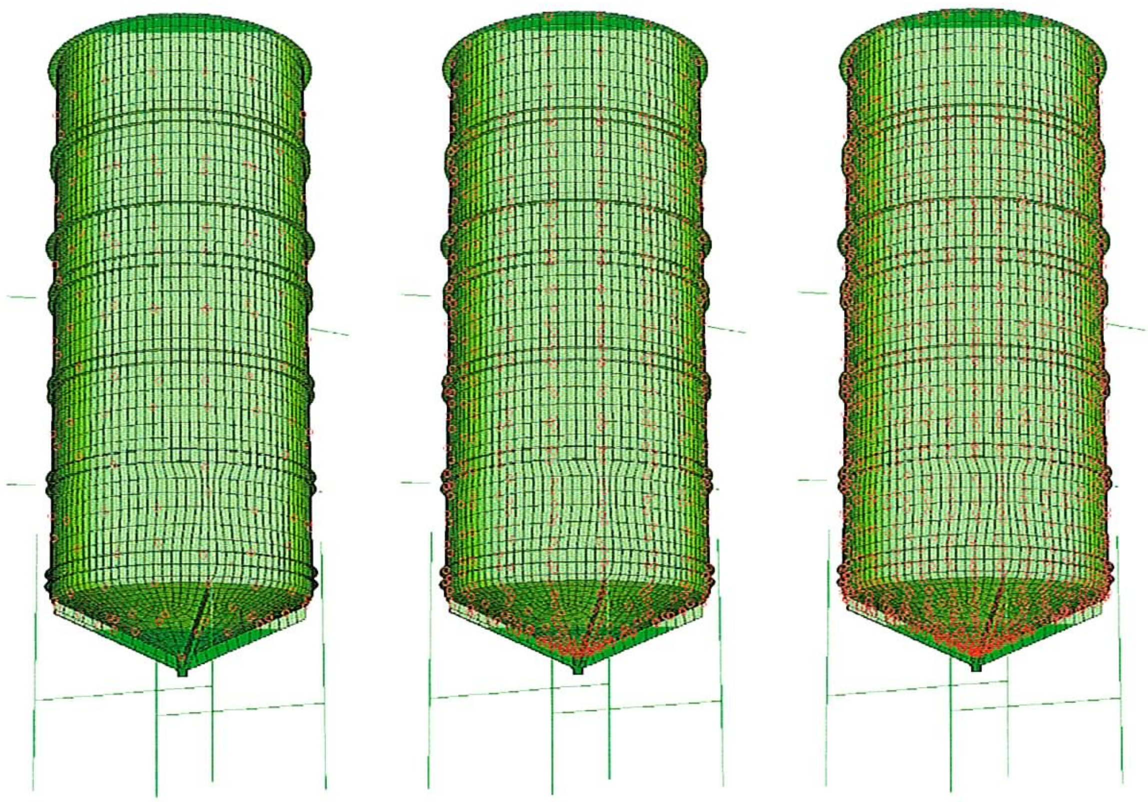

Node Set 1 *Node Set 2* *Node Set 3*

Figure 19. Retained nodes in different substructures.

Table 2. Different substructures of the FE model of the pool. Substructure 3 is used in the FSI analysis with the ES-FSI code. The retained nodes in the different substructures are shown in Figure 19.

Substructure	Retained nodes	Retained DOF	Number of MDOF
1	Node Set 1	Translations	369
2	Node Set 1	Translations + rotations	738
3	Node Set 2	Translations	1443
4	Node Set 2	Translations + rotations	2886
5	Node Set 3	Translations + rotations	5856
6	Unconstrained nodes on coupling surface	Translations	15177

3.4.1 Computational Cost of the Substructure Analysis

Memory requirement and analysis time needed to generate stiffness and mass matrices for the different substructures are listed in Table 3. The corresponding values for computational cost of a linear static analysis are included for comparison. Memory requirement for the substructure analyses is plotted as a function of the number of MDOF in Figure 20.

Memory requirement and analysis time for the substructure analyses are greatly larger than for a linear static case. According to Figure 20, memory requirement increases rapidly as the number of MDOF is increased. Memory requirement for the stiffness and mass matrices of a substructure increases proportional to the second power of the number of MDOF, since the matrices are fully populated. Also, the matrices of a substructure are presented in double precision in ABAQUS. Double precision takes 8 bytes of memory per number, i.e., twice as much as single precision accuracy. If the symmetry of the matrices is accounted for, the total number of elements in the stiffness and mass matrices in the case of Substructure 6 is approximately 2.3×10^8. Memory requirement of storing these elements in double precision is about 1840 Mbytes. Approximately 6120 Mbytes is needed for the analysis for Substructure 6. It is clear that memory requirement for the substructure analysis becomes easily excessive, even though in this case the number of elements in the FE model is modest.

Table 3. Computational cost of different substructure analyses and corresponding linear static analysis. Substructure 3 is used in the FSI analysis with the ES-FSI code.

Substructure	Memory requirement [Mbytes]	Analyses time [s]
1	82	183
2	90	356
3	168	1348
4	293	4920
5	1002	-
6	6120	-
Linear static analyses	31	25

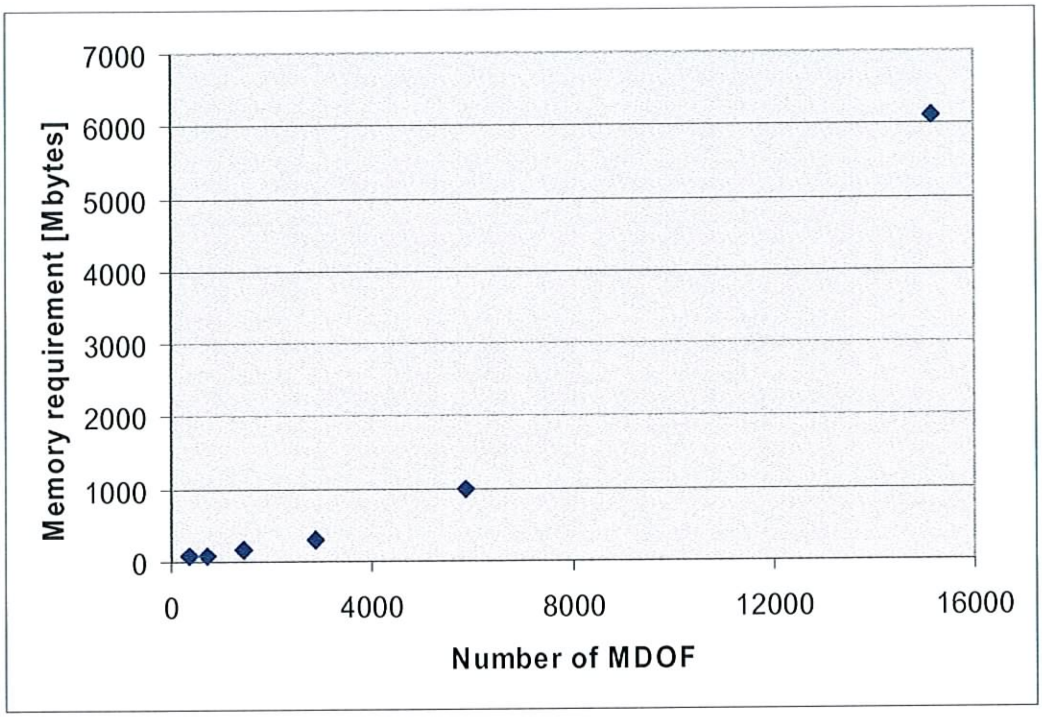

Figure 20. Memory requirement of substructure analyses with different numbers of MDOF.

3.4.2 Eigenvalue Extractions

Eigenvalue extraction is conducted for substructures 1 - 4 (see Table 2) and the original FE model of the pool. Figure 21 shows the relative error in frequency for the first 17 eigenmodes for substructures 1 - 4. The error is plotted as a function of eigenfrequency of the original FE model. The relative error in frequency is expectedly larger for high frequency eigenmodes. It might be concluded from Figure 21, that the last few frequencies for substructures 1 and 2 represent different eigenmodes, but this is not the case. The lowest eigenfrequencies of the substructures are higher than those of the original FE model. This is due to displacement constraints imposed in substructuring (Cook et al., 2002). It is also evident from Figure 21, that retaining rotational DOF has little effect on the accuracy of representing the lowest eigenmodes as indicated in Cook et al. (2002). The improvement in accuracy is minimal for the substructures with rotational DOF, but the number of MDOF is doubled. At least in this sense, retaining only translational DOF of the pool wall is reasonable.

Table 4 shows the frequency and generalized mass for the first 50 eigenmodes of the original FE model of the pool and Substructure 3. Selected eigenmodes of the original FE model and Substructure 3 are compared in Figure 22. For modes 1 - 17, i.e., for frequencies up to about 100 Hz, the agreement is good as indicated in Figure 22, although the selection of MDOF is quite sparse. It should be noted that comparison of the values in Table 4 with same mode number is not valid for high-frequency modes. This is because some higher modes present in the original model are not represented by the substructure at all.

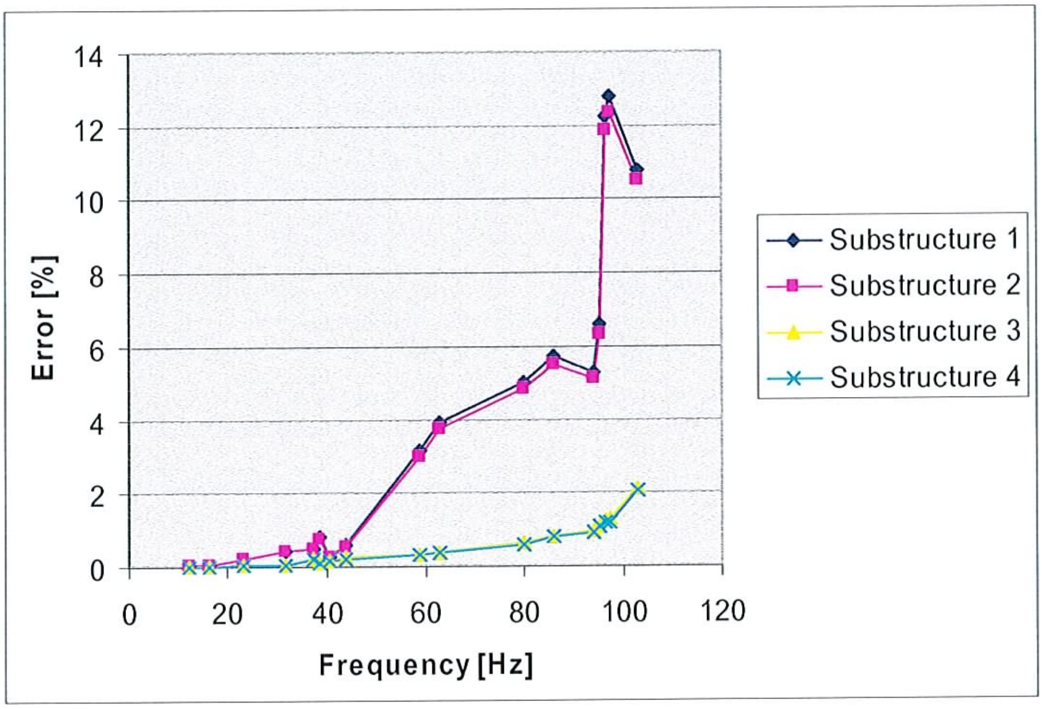

Figure 21. Relative error in frequency for the first 17 eigenmodes for substructures 1 - 4 as a function of eigenfrequency of the original FE model.

Table 4. Frequency and generalized mass of the first 50 eigenmodes of the original FE model and Substructure 3 (see Table 2).

Mode	Frequency [Hz]		Generalized mass	
	Original model	Substructure 3	Original model	Substructure 3
1	12,25	12,25	1188,9	1213,7
2	16,21	16,21	1496,4	1637,1
3	22,92	22,93	300,0	365,4
4	31,82	31,85	290,9	333,2
5	37,28	37,36	781,2	774,7
6	38,44	38,48	299,8	374,3
7	40,49	40,55	1776,7	1815,3
8	43,81	43,92	688,5	688,1
9	58,65	58,84	136,6	208,8
10	62,77	63,01	147,2	227,7
11	79,88	80,38	245,1	359,7
12	85,75	86,44	213,1	249,3
13	94,10	95,02	301,5	316,6
14	95,22	96,27	310,7	504,4
15	96,62	97,85	136,3	194,1
16	97,46	98,72	107,7	155,1
17	103,08	105,28	62,8	117,6
18	106,04	111,19	59,9	40,6
19	112,06	115,12	55,0	235,1
20	113,11	120,93	38,3	30,9
21	113,82	121,89	58,7	36,8
22	118,72	128,38	40,7	214,4
23	120,59	133,58	83,1	17,6
24	124,01	136,89	84,7	42,4
25	125,75	139,02	132,8	20,4
26	129,29	140,02	38,8	16,8
27	131,62	141,45	30,9	25,5
28	133,75	142,16	183,5	170,9
29	135,61	143,98	105,4	38,8
30	137,62	144,72	55,5	183,6
31	137,87	148,39	78,8	44,3
32	139,24	151,94	70,7	59,4
33	141,04	152,61	34,7	43,7
34	142,11	156,42	122,9	35,9
35	145,80	160,01	26,5	68,8
36	146,94	162,34	15,1	154,7
37	147,54	163,21	29,7	91,6
38	147,99	169,01	60,2	84,2
39	150,32	174,27	23,9	7,2
40	151,13	175,54	45,5	181,2
41	151,59	177,44	32,0	12,8
42	155,67	177,50	33,6	12,4
43	155,68	178,33	34,1	94,2
44	156,74	178,65	86,6	13,4
45	156,86	180,68	36,5	17,7
46	156,86	180,89	36,4	17,0
47	157,22	180,95	27,4	30,0
48	157,98	182,89	59,2	32,8
49	158,82	183,17	33,8	17,9
50	158,82	183,68	33,8	43,2

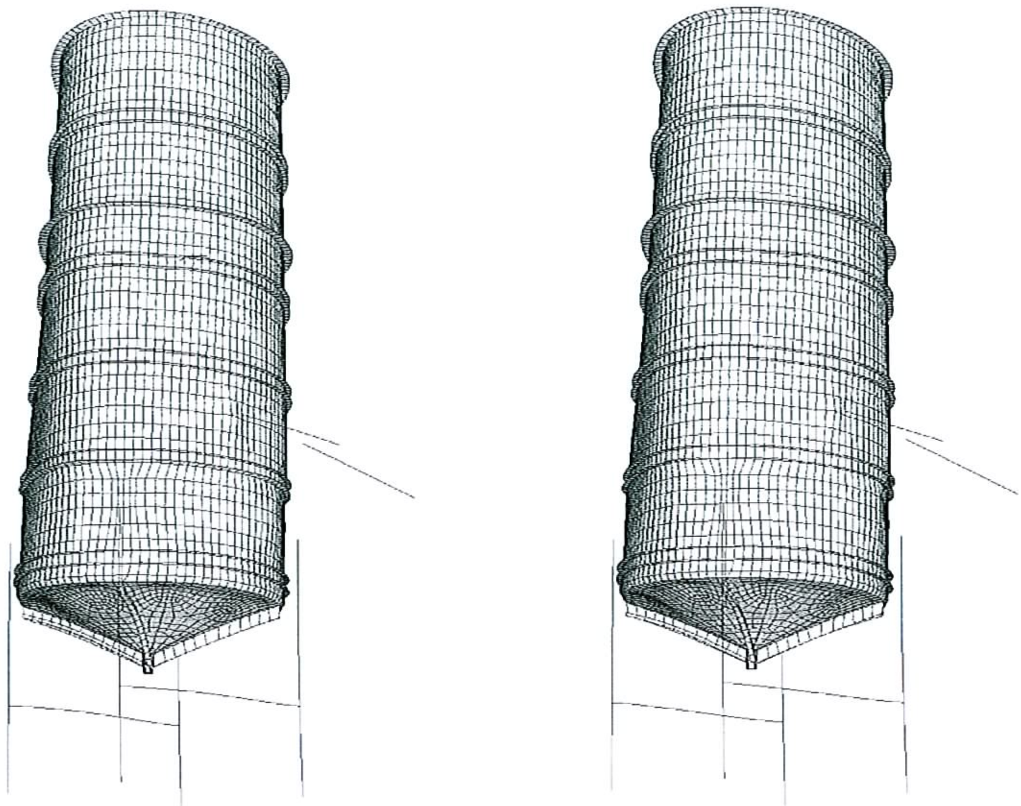

Mode 7

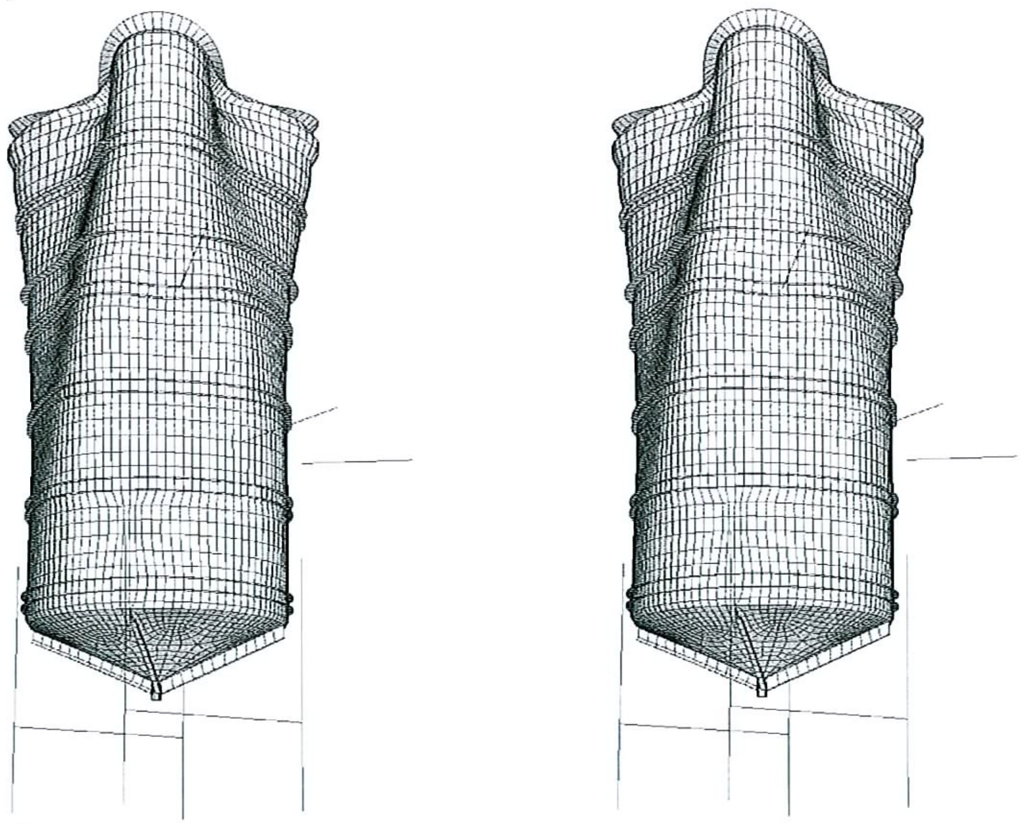

Mode 10

Figure 22. Selected eigenmodes of the pool. Original FE model on the left, Substructure 3 on the right. Mode number is presented under the plots (continues on the following page). The frequency and generalized mass of the modes are presented in Table 4.

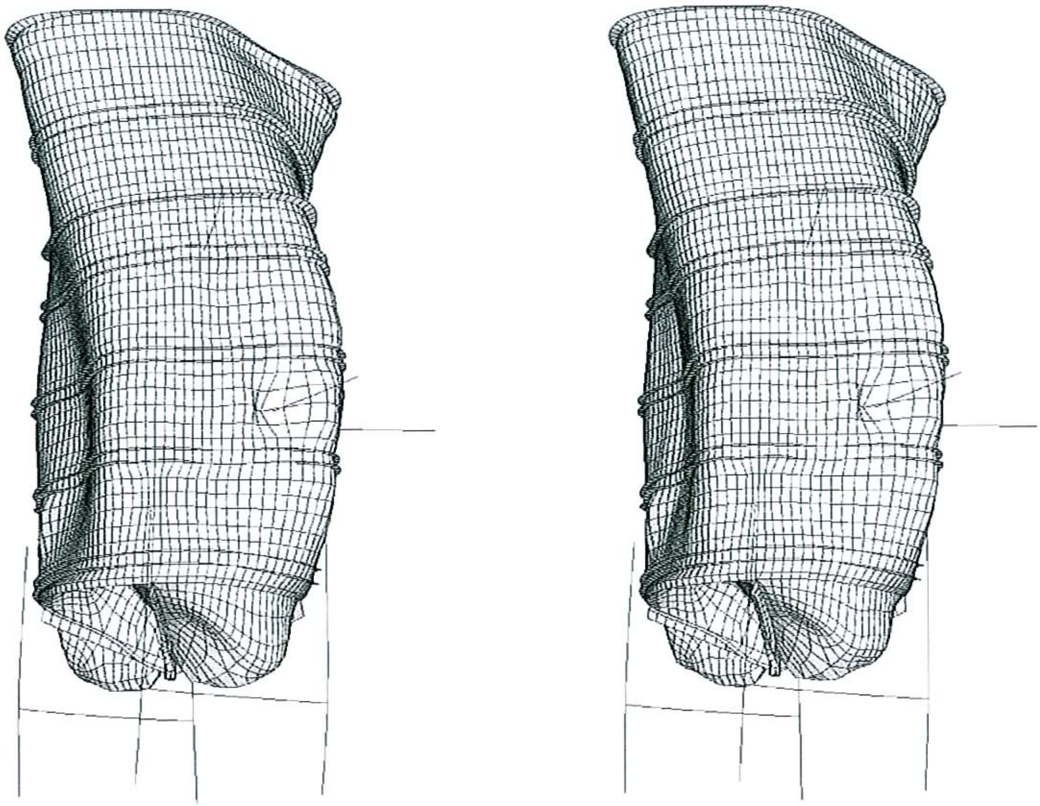

Mode 13

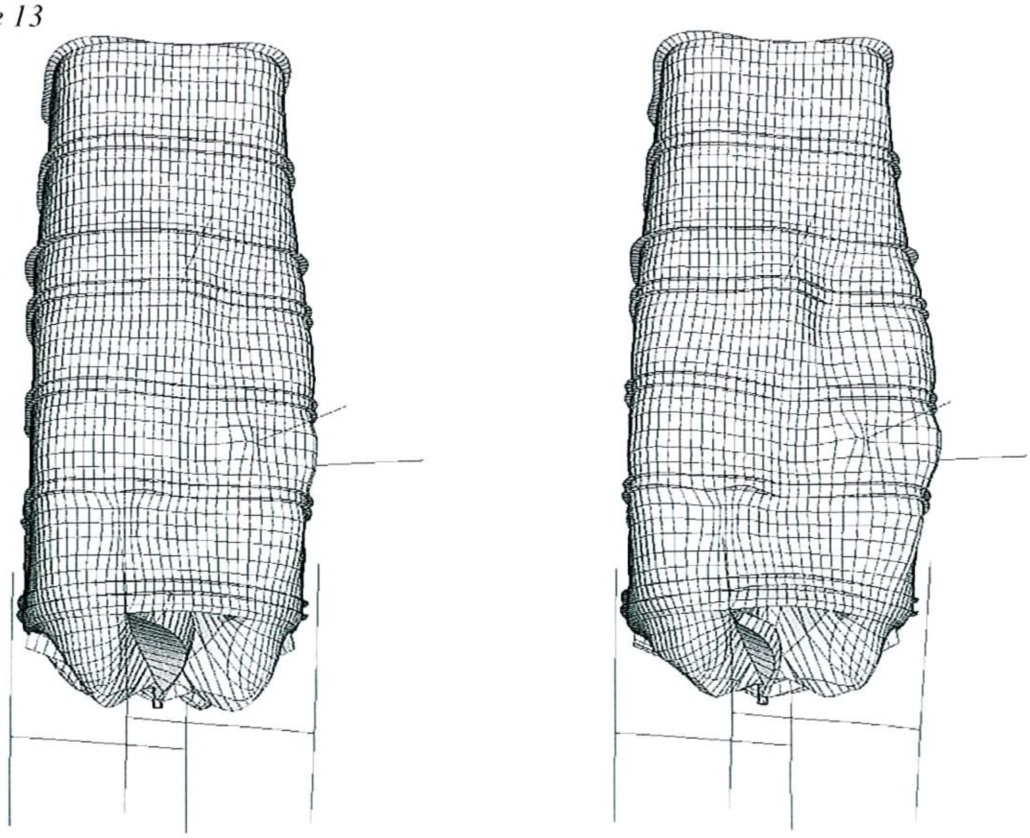

Mode 17

Figure 22. Continues from the previous page.

3.5 Fluid-structure Interaction Calculation

Two different fluid-structure interaction simulations were performed with Star-CD and ES-FSI for the water pool of the POOLEX experiment. First, the water pool was studied under the rapid application of the hydrostatic load of water. Second, a rapid collapse of a steam bubble in the pool was investigated. The mesh movement macro for the present calculations was prepared by David Eby, CD adapco Group.

3.5.1 Pool under Steady Load Caused by Water

The loading of the pool wall caused by the hydrostatic pressure of water was first solved by coupled fluid-structure interaction simulation. The load of the water was applied to the pool structures instantaneously at time $t = 0$, and the fluid pressure and the motion of the pool was solved for a time of 20 s. In order to find the stationary state, the motion was damped artificially by adding a large material damping for the structure. In the simulation with the steady hydrostatic load, the values $\alpha = 400$ 1/s and $\beta = 0$ were chosen for the Rayleigh damping coefficients.

The structural results due to the steady load are analysed in Section 3.6.1.

3.5.2 Fluid-structure Interaction Analysis of a Collapsing Bubble

The pressure transient caused by a rapid collapse of a steam bubble was analysed by modelling the collapse with the aid of the analytical model described in Sec. 2.3. The results of the fluid-structure interaction analysis were compared to the results obtained previously by assuming a rigid wall (Timperi et al., 2004).

The relative pressure in the pool is illustrated in Fig. 23 during the bubble collapse in the ES-FSI calculation and in the calculation with a rigid wall. First, an under pressure is formed in the pool, when the collapse of the bubble starts near the pipe exit. In the ES-FSI simulation, the pressure is higher during the under pressure stage than in the simulation with rigid wall.

In the time interval between $t = 14$ and 15 ms, a spherical overpressure wave hits the pool wall. The pressure transient propagates from the vicinity of the pipe exit towards the pool wall at the speed of sound in water, i.e., $v_a = 1470$ m/s. In Fig. 23, the amplitude of the pressure transient is higher in the simulation with the rigid wall than in the ES-FSI simulation. It is interesting to note that the pressure transient occurs slightly later in the ES-FSI simulation than in the simulation with a rigid wall.

At the end of the bubble collapse, between $t = 22$ and 23 ms, a second overpressure wave propagates from the vicinity of the pipe towards the pool wall. This pressure transient is initiated, when water flowing towards the bubble centre is decelerated and compressed at the end of the collapse. In this stage, the differences in the pressure amplitudes are not very significant in the ES-FSI and in the rigid wall simulations.

In Fig. 24, examples of wall pressure loads are shown in the FSI simulation and in the rigid wall simulation. The form of the spherical pressure wave is also clearly visible in the wall loads.

In the simulation of the bubble collapse, the CFD simulation was performed for two seconds applying only the hydrostatic load on the structures in order to obtain a stationary state. After two seconds, the mass sink modelling the bubble collapse was applied. Since no artificial Rayleigh damping was applied in this simulation, the pool structures were not in stationary state in the beginning of the bubble collapse. The low frequency oscillation of the structures hampers the interpretation of the results in the beginning of the bubble collapse. The rapid end phase of the collapse can, however, be resolved from the low frequency motion of the pool walls.

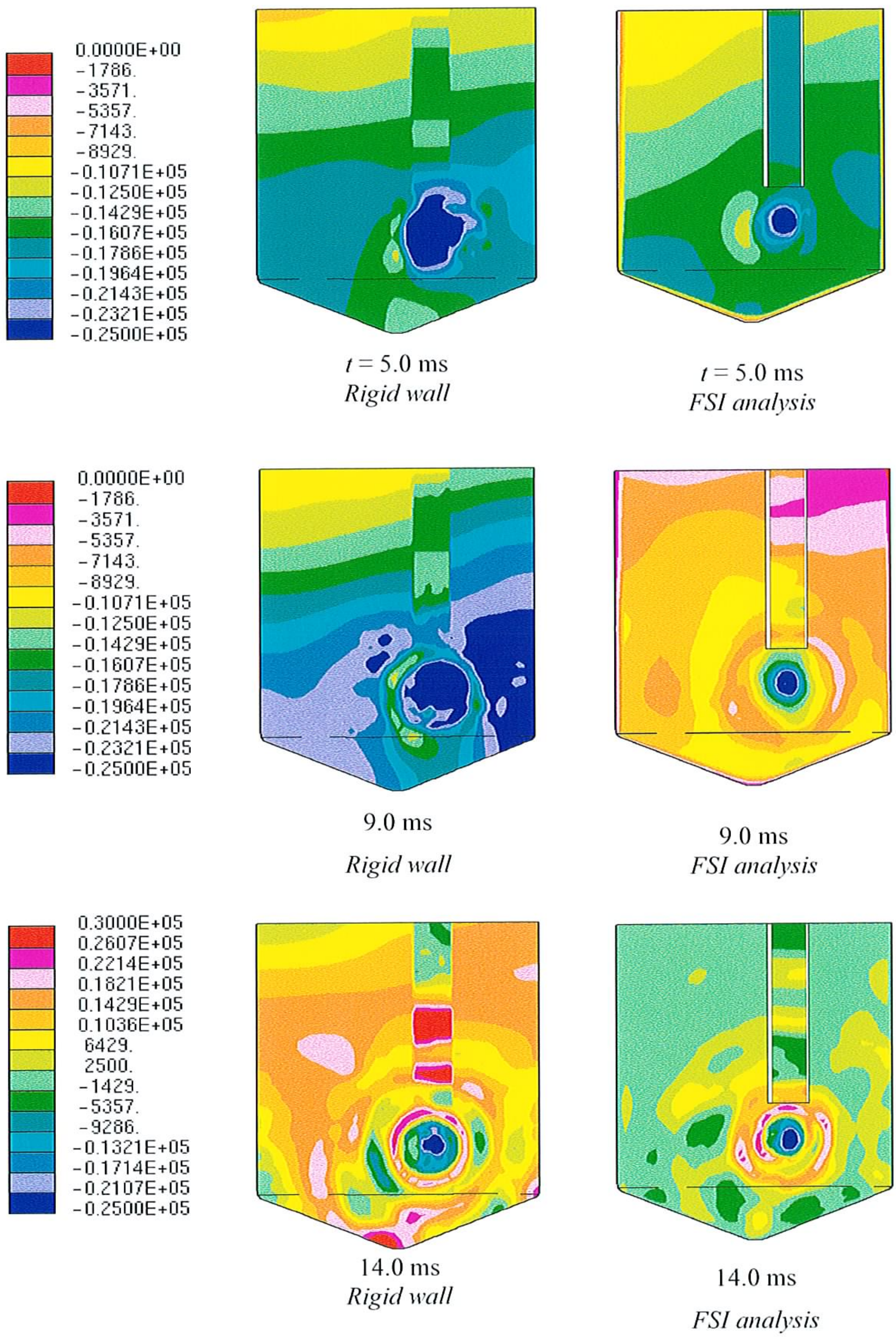

Figure 23. Relative pressure (Pa) during the collapse of a void bubble at different instants of time. The hydrostatic pressure and the atmospheric pressure are not included in the values shown (Continues on the following page).

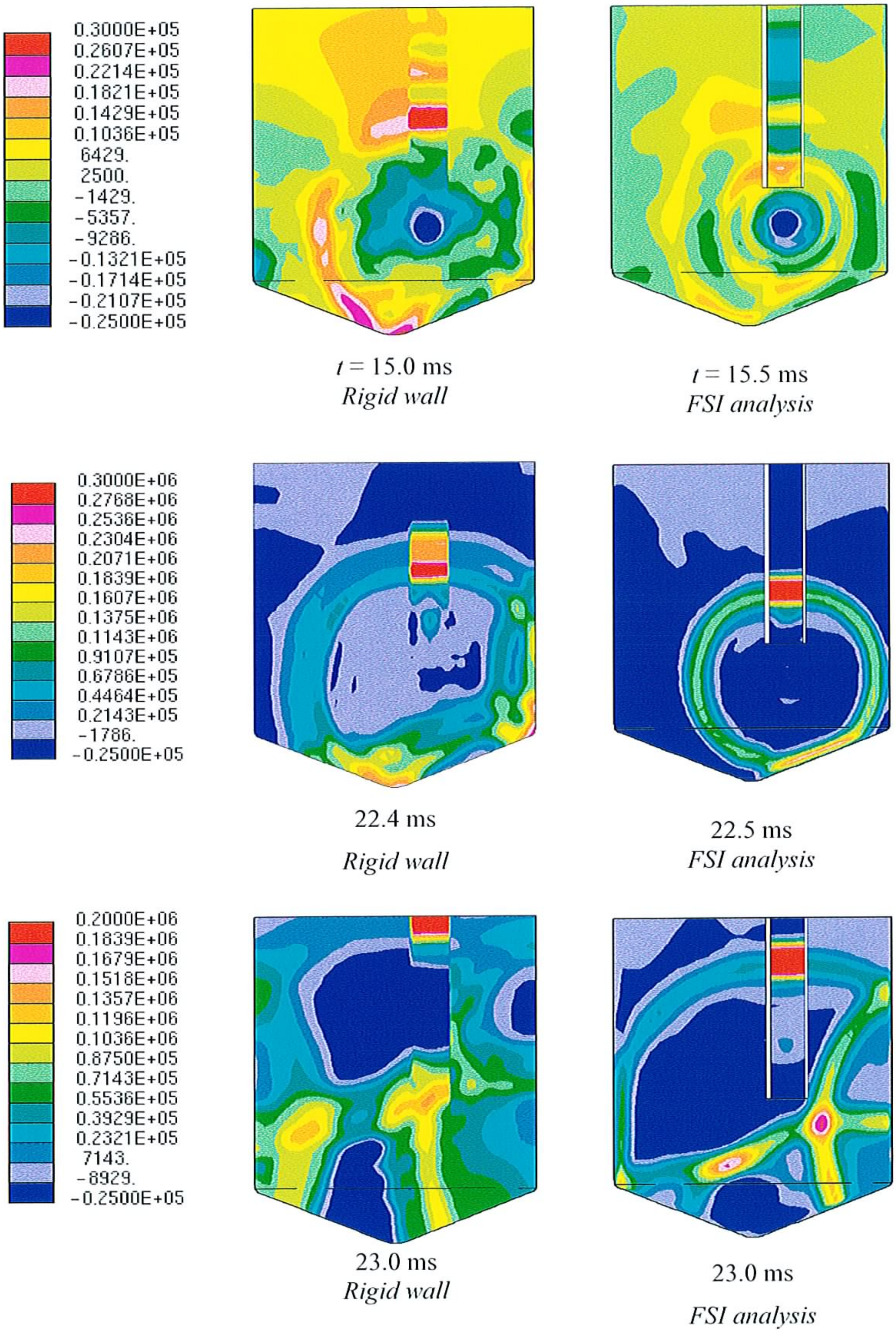

Figure 23. Relative pressure (Pa), continues from the previous page.

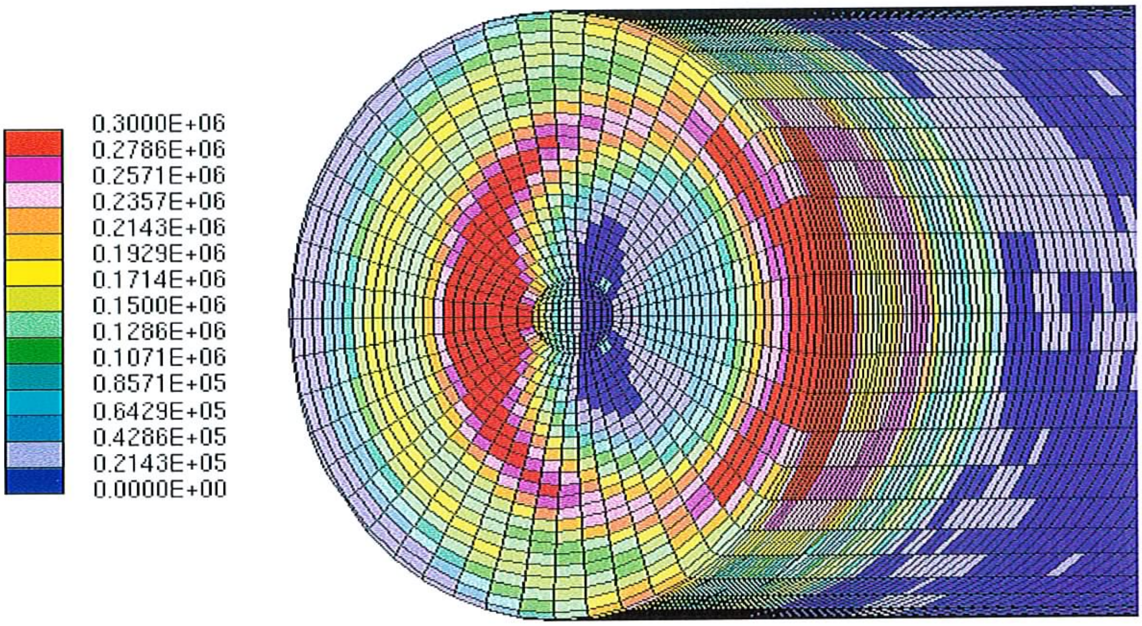

t = 22.4 ms
Rigid wall

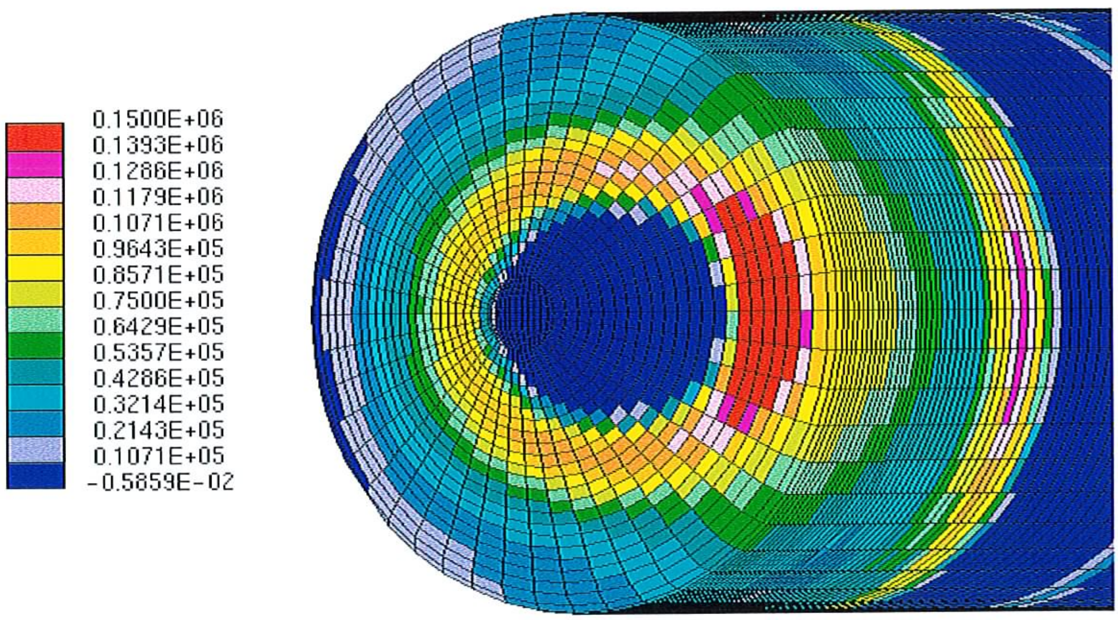

24.0 ms

FSI analysis

Figure 24. Relative wall pressure (Pa) obtained by assuming a rigid wall and by performing FSI analysis.

3.6 Post-analysis of the pool structures

Structural results for the FSI analysis of the static state of the pool under hydrostatic load are presented in Section 3.6.1. Structural results of the dynamic calculation of the condensation induced water hammer are presented in Section 3.6.2.

3.6.1 Static Results

In this analysis, a large material damping is included to the structural model as discussed in Sect. 3.5.1. Some initial oscillations of the pool occur after the instantaneous application of the gravity load, but a static state is obtained well within the 20 s duration of the calculation. For comparison, a conventional static analysis of the original FE model is conducted by using a corresponding hydrostatic pressure load.

Figure 25 shows contour plots of inner wall von Mises stress distribution and deformed shape of the pool due to hydrostatic pressure for the static and FSI analysis. The deformation scale factor in Figure 25 is 150. Maximum von Mises stresses on the inner wall are approximately 127 and 138 MPa for the static and FSI case, respectively. The maximum stresses are located at the rounding of the pool bottom wall in both cases. The results of the FSI analysis show however quite uneven distribution of displacements and stresses, which is due to the sparse choice of MDOF. Deformations in the cylinder part of the pool are also greatly overestimated by the FSI analysis. Maximum displacement normal to the wall at the cylinder of the pool is approximately 2 mm for the FSI case. The corresponding maximum displacement for the static analysis is approximately one order of magnitude smaller. Differences in deformations at the bottom of the pool are quite small between the cases. In the pool wall, the overestimation of the displacements outwards and the unrealistic displacements inwards are due to the fact that the wall is being pushed outwards only at the retained nodes. It should be noted that because the FSI calculation takes into account only the displacements of the retained nodes, the interpolation of the positions of the CFD mesh vertices are not affected by the inward deflections. According to the results, the selection of MDOF is too coarse for the FE model.

Vertical displacements of the pool bottom centre and lower ends of the vertical supports in both cases are listed in Table 5. The displacements of the support ends are due to the disc springs under the supports. The displacements of the support ends are approximately 5.8 – 10.6 % larger for the FSI analysis. According to this, the vertical resultant force due to the interpolated pressures of the FSI analysis is somewhat too large. Some error in the interpolation is expected, since a small number of MDOF is used.

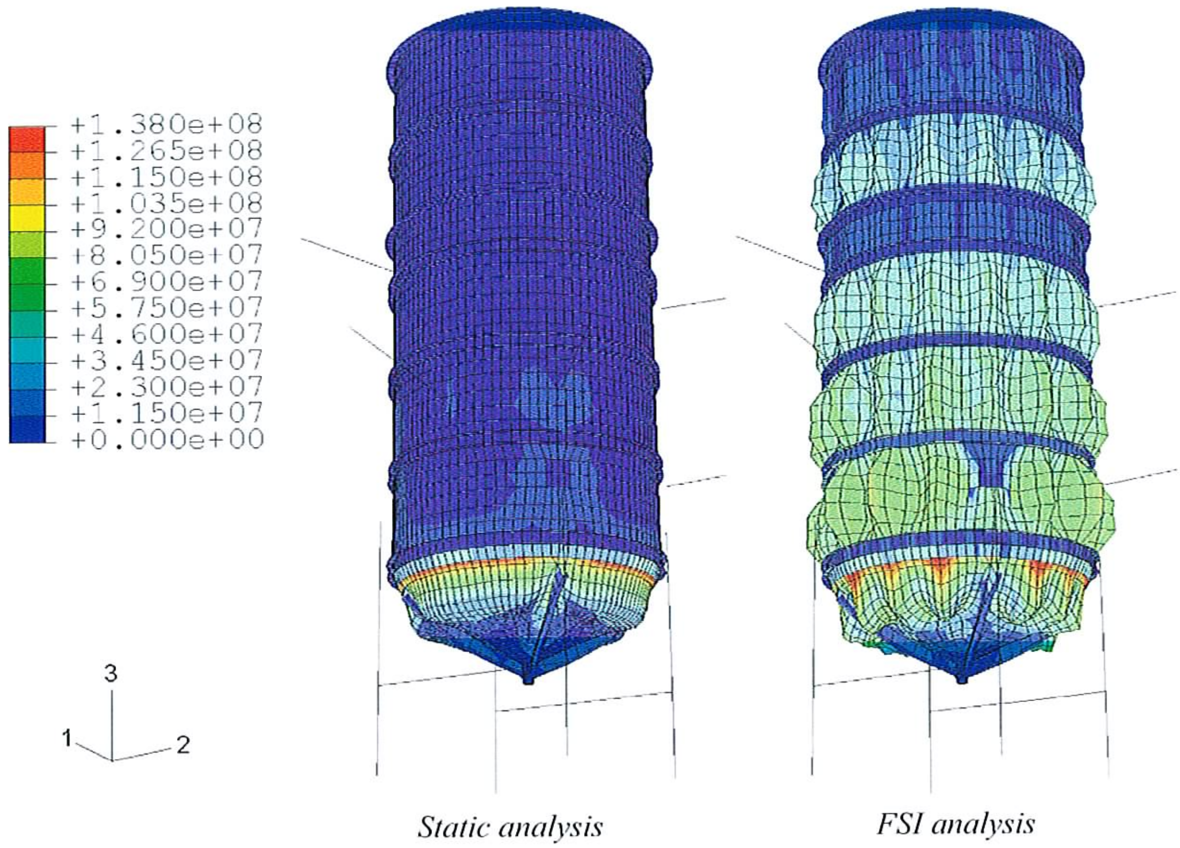

Figure 25. Von Mises stress (Pascal units in legend) distribution on the inner wall of the pool. Maximum stress is approximately 127 MPa in the static analysis and 138 MPa in the FSI analysis. The deformation scale factor is 150.

Table 5. Vertical displacements of the pool bottom centre and lower ends of the vertical supports in the static and FSI analysis.

Location	Static analysis [mm]	FSI analysis [mm]	Error [%]
Bottom Centre	-2.40	-2.47	3.0
Support End 1	-1.26	-1.39	10.5
Support End 2	-1.27	-1.36	7.6
Support End 3	-1.27	-1.41	10.6
Support End 4	-1.27	-1.34	5.8

3.6.2 Dynamic Results

Stationary state of the pool due to mere gravity load was not obtained in the dynamic analysis, as discussed in Section 3.5.2. Low frequency oscillation of the pool due to incorrect initial conditions occurs at the beginning of the FSI calculation, which affects the behaviour of the structure considerably.

Contour plots of inner wall von Mises stress distribution and deformed shape of the pool at different instants of time are shown in Figure 26. The deformation scale factor in Figure 26 is 150. The distributions of displacements and stresses are similar to the case where the static state of the pool is calculated (see Fig. 25). Despite the facts that too few MDOF are used and the initial state for the analysis is not a static one, the behaviour of the pool seems qualitatively correct.

The deformations of the pool are partly due to the non-static initial conditions and thus only partly due to the condensation induced water hammer. Therefore, comparison of the structural results of the dynamic FSI calculation to the uncoupled case in Timperi et al. (2004) is not conducted.

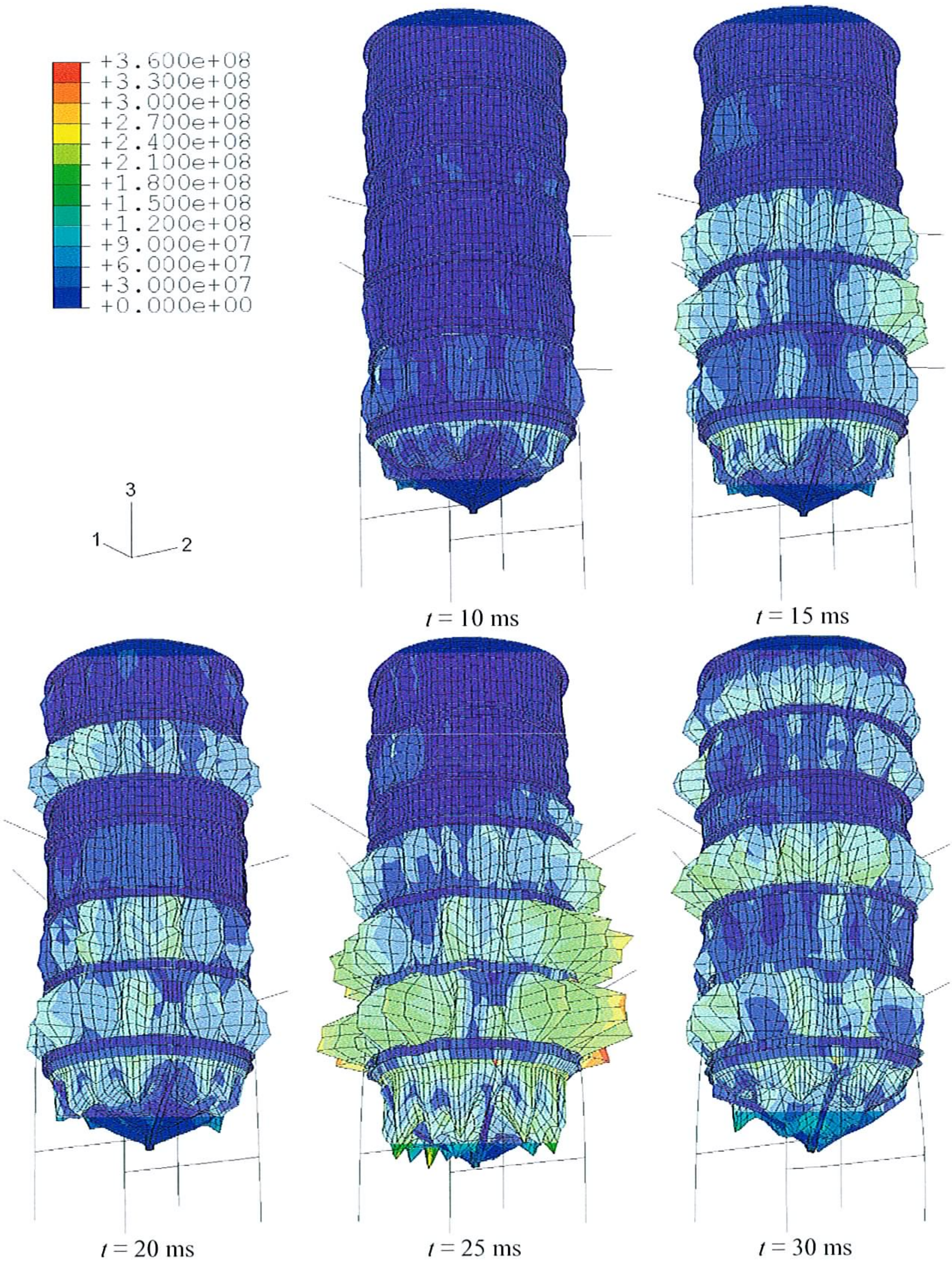

Figure 26. Von Mises stress (Pascal units in legend) distribution on the inner wall of the pool at different instants of time. The deformation scale factor is 150.

4 Summary and Conclusions

Methods for estimating pressure loads in a water pool during steam injection have been investigated. The Method Of Images (MOI) for calculating the pressure loads during a steam bubble collapse was implemented and tested for the POOLEX experiment at the Lappeenranta University of Technology (Laine and Puustinen, 2004). First version of homogeneous two-phase model was implemented for Star-CD CFD code. The homogeneous two-phase model was tested in a quasi-stationary situation, where the steam that was blown down into a water pool was condensing inside the vertical blowdown pipe. Finally, a coupled fluid-structure interaction calculation was performed with Star-CD and ABAQUS which were coupled with the ES-FSI code. The motion of the wall during a rapid bubble collapse was taken into account during the CFD calculation by using pre-calculated mass and stiffness matrices of the structure.

The method of images was successfully applied to calculating rapid collapse of a bubble in a water pool. The most difficult part of this method is, however, choosing the pressure source terms for the model. In the present work, the source terms were chosen based on the experimental results obtained in the POOLEX experiment. Further investigation of the source terms is necessary in order to use the method of images as a predictive tool.

The homogeneous two-phase model was applied to steam blowdown into a water pool in the quasi-stationary situation, where the steam is condensed already in the blowdown pipe. The transient simulations have so far suffered from convergence problems, which seem to originate from the structure of the PISO solver of Star-CD. If these problems cannot be solved, alternative methods for modelling steam-water mixture must be considered.

Fluid-structure interaction analysis by using Star-CD and ABAQUS was performed for the POOLEX experiment by using ES-FSI for solving the motion of the pool in the CFD calculation. Two different situations were considered. First, the structural results were analysed when the hydrostatic load caused by water was instantaneously applied to the pool. After initial oscillations, the pool achieved a stationary steady state. Second, the pool was investigated during a rapid condensation of a steam bubble which was modelled with a mass sink in a single-phase CFD calculation. The pressure loads obtained with ES-FSI were compared to previous analysis, where rigid pool wall was assumed.

Accuracy of a substructure in representing the most important dynamic modes of the structure may be quite good even with a relatively small number of MDOF. However for the analyses with ES-FSI, the number of MDOF probably has to be larger for most cases. This is due to the accuracy requirements of interpolating the pressures and displacements and representing deformations of the structure. Ideally, all translational DOF on the coupling surface would be selected as MDOF. This means, that the accuracy of representing the dynamic modes will usually not be the main concern. Economy in the size of the substructure would be achieved by retaining DOF only in selected directions, e.g. only horizontal displacements at the wall of a vertical cylinder would be retained.

Post-analysis of the pool structures was conducted for the both FSI calculations. In the pool wall, the displacements were greatly overestimated and were partly unrealistic. The deformations and stresses of the pool wall showed uneven distributions. These were due to the fact, that a small number of MDOF were used. Otherwise, the results of the both FSI analysis were reasonable. The vertical resultant force due to the static load of the water was relatively close to a more accurate conventional analysis. Detailed comparison of the dynamic

FSI calculation to the earlier uncoupled case was not possible due to different initial conditions in the analyses. Accurate FSI analysis of the pool would require a denser choice of MDOF than was used. It also remains to be studied, whether a coarser FE mesh with all necessary nodes retained would yield better results.

Substructure analyses are costly in terms of memory requirement and computer analysis time, if the number of MDOF is large. Retaining all unconstrained nodes on the coupling surface of the pool examined in this work would require over 6 Gbytes of memory. Yet the size of the FE model was quite moderate. The maximum memory available for running ABAQUS 6.4 or 6.5 is 3 Gbytes on 32-bit platforms (ABAQUS, 2003b; ABAQUS). Performing the analysis on a 64-bit machine would allow larger memory allocation. However, the memory requirement of substructuring increases proportional to the second power of the number of MDOF. Thus, memory requirement needed to generate the matrices for a substructure may easily become excessive for large-scale applications. For cases including a large structural model, a different solution from ES-FSI may have to be used.

Often in accident analyses of nuclear industry, large structural models are required and accurate structural response is of main interest. In addition, material, geometric and contact nonlinearities are often found, i.e., full capabilities of the FE code is needed. Furthermore, the longer analysis time in the direct coupling of CFD and structural analysis codes is not the main concern. For these kinds of cases MpCCI (MpCCI Team, 2002), or similar tool, has to be used. Another advantage with MpCCI is the possibility of performing FSI analysis, which includes heat transfer between the fluid and the structure.

In the earlier work, a large-break LOCA was analysed in a pressurised-water reactor with a one-directional FSI calculation by Pättikangas and Timperi (2004). The behaviour of the core barrel of the reactor was analysed by using a relatively simple structural model containing 2689 shell elements. The number of nodes in the model was 2785. Retaining all necessary DOF of this model is possible, i.e., accurate FSI analysis of the same case with ES-FSI can be carried out. Later, a more detailed FE model is required and for example the MpCCI code would be more efficient.

References

ABAQUS Theory Manual. 2003a.Version 6.4. Hibbit, Karlsson & Sorensen Inc. RI.

ABAQUS Analysis User's Manual. 2003b.Version 6.4. Hibbit, Karlsson & Sorensen Inc. RI.

ABAQUS Version 6.5 Technical Notes. URL: http://www.hks.com.

Anderson, E.I., 2000. The method of images for leaky boundaries. Advances in Water Resources 23, 461-474.

Anon., 2001. Star-CD version 3.15, Methodology, CD adapco Group.

Calonius, K., Pättikangas, T. and Saarenheimo, A., 2003. Numerical analyses of a water pool under loading caused by large air and steam bubbles, VTT Industrial Systems, Project Report BTUO72-031106, Espoo, Finland, 43 p.

Cook, R., Malkus, D., Plesha, M. and Witt, R., 2002. Concepts and applications of finite element analysis. Wiley & Sons, Inc. ISBN 0-471-35605-0.

Giencke E., 1981. Pressure distribution due to a steam bubble collapse in a BWR pressure suppression pool. Nuclear Engineering and Design 65, 175-196.

Laine, J., 2002. Condensation pool experiments with non-condensable gas, Lappeenranta University of Technology, Research Report TOKE-2/2002, 46 p. + app. 14 p.

Laine J. and Puustinen M, 2003. Preliminary condensation pool experiments with steam using DN80 and DN100 blowdown pipes. POOLEX 4/2003 research report, Lappeenranta University of Technology, Nuclear Safety Research unit.

Laine J. and Puustinen M, 2004. Preliminary condensation pool experiments with steam using DN200 blowdown pipe. POOLEX 1/2004 research report, Lappeenranta University of Technology, Nuclear Safety Research unit.

Li P. and Uren N. F. U., 1997. Analytical solution for the point source potential in an anisotropic 3-D half-space I: two-horizontal-layer case. Mathl. Comput. Modelling 26, No. 5 9-27.

MpCCI Team, 2002. Mesh-based parallel Code Coupling Interface, Specification of MpCCI version 1.3, Fraunhofer Institute for Algorithms and Scientific Computing, Sankt Augustin, Germany, 125 p.

Pättikangas, T. and Pokela H., 2003. Wall-loadings caused by large air bubbles injected in a water pool, VTT Processes, Project Report PRO4/T7534/02, Espoo, Finland, 28 p.

Pättikangas T. and Timperi A., 2004. CFD and structural analysis of the pressure transient in the beginning of a large-break LOCA in a PWR, VTT Industrial Systems, Research Report BTUO72-041302, Espoo, Finland, 41 pp.

RELAP5/MOD1 Code Manual, 1980. Vol 1 System Models and Numeric Methods, U.S. Department of Energy.

Timperi A., Pättikangas T., Calonius K., Tuunanen J., Poikolainen J. and Saarenheimo A., 2004. Numerical analyses of a water pool under loadings caused by a condensation induced water hammer, VTT Industrial Systems, Research Report BTUO72-031198, Espoo, Finland, 66 pp.

TRAC-M/FORTRAN90 Theory Manual, 2000. Los Alamos National Laboratory and Pensylvania State University.

Wood B. D., Sun W-J. and Domoto G. A., 1980. Determination of pressure fields in a BWR suppression pool by means of Green's function and comparison with method of images and a finite difference solution. Nuclear Engineering and Design 61, 153-161.

Title	Fluid-Structure Interaction Analysis of a Water Pool under Loading Caused by a Condensation-Induced Water Hammer
Author(s)	Timo Pättikangas, Antti Timperi, Jarto Niemo & Timo Narumo
Affiliation(s)	VTT Industrial Systems, Finland
ISBN	87-7893-163-0 *Electronic report*
Date	April 2005
Project	NKS_R_2002_1
No. of pages	56
No. of tables	5
No. of illustrations	26
No. of references	19

Abstract

A coupled fluid-structure interaction calculation was performed with Star-CD and ABAQUS, which were coupled with the ES-FSI code. The motion of the wall of a test pool during a rapid bubble collapse was solved and taken into account during the CFD calculation. A fluid-structure interaction analysis was also conducted, in which the stationary state of the pool due to a gravity load was calculated. In addition, methods for estimating pressure loads in a water pool during steam injection were investigated. The Method of Images (MOI) for calculating the pressure loads during a steam bubble collapse was implemented and tested for the POOLEX experiment. The first version of the homogeneous two-phase model was implemented for the Star-CD CFD code and tested in the quasi-stationary situation, where the steam that was blown down into a water pool was condensing inside the vertical blowdown pipe.

Key words CFD, FE, FSI, condensation water hammer, pressure load

Available on request from the NKS Secretariat, P.O.Box 49, DK-4000 Roskilde, Denmark.
Phone (+45) 4677 4045, fax (+45) 4677 4046, e-mail nks@nks.org, www.nks.org